

How much water is there within calcium silicate hydrates? Probing water dynamics by Inelastic Neutron Scattering and Molecular Dynamics Simulations

Zhanar Zhakiyeva, Valérie Magnin, Agnieszka Poulain, Sylvain Campillo, María Pilar Asta, Rogier Besselink, Stéphane Gaboreau, Francis Claret, Sylvain Grangeon, Svemir Rudic, Stéphane Rols, Mónica Jiménez-Ruiz, Ian C. Bourg, Alexander E.S. Van Driessche, Gabriel J. Cuello, Alejandro Fernández-Martínez

Corresponding Authors

Zhanar Zhakiyeva - University of Grenoble Alpes, University of Savoie Mont Blanc, CNRS, IRD, IFSTTAR, ISTerre, 38000 Grenoble; Institut Laue-Langevin, 38042 Grenoble, France; Department of Chemical and Materials Engineering, School of Engineering and Digital Sciences, Nazarbayev University, Kabanbay Batyr Ave. 53, Astana, 010000, Kazakhstan Phone: +77780665182; Email: zhanar.zhakiyeva@nu.edu.kz

Alejandro Fernández-Martínez – University of Grenoble Alpes, University of Savoie Mont Blanc, CNRS, IRD, IFSTTAR, ISTerre, 38000 Grenoble, France; Phone: +33(0)476635197; Email: alex.fernandez-martinez@univ-grenoble-alpes.fr

Ian C. Bourg – Department of Civil and Environmental Engineering and High Meadows Environmental Institute, Princeton University, Princeton, New Jersey 08544, United States; Email: bourg@princeton.edu

Alexander E. S. Van Driessche – Instituto Andaluz de Ciencias de la Tierra (IACT), CSIC – University of Granada, Armilla, Granada E-18100, Spain; Email: alexander.vd@csic.es

Authors

Gabriel J. Cuello - Institut Laue-Langevin, 38042 Grenoble, France;

Valérie Magnin – University of Grenoble Alpes, University of Savoie Mont Blanc, CNRS, IRD, IFSTTAR, ISTerre, 38000 Grenoble;

Sylvain Campillo – University of Grenoble Alpes, University of Savoie Mont Blanc, CNRS, IRD, IFSTTAR, ISTerre, 38000 Grenoble;

Svemir Rudic - ISIS Neutron & Muon Source, STFC Rutherford Appleton Laboratory, Chilton, Didcot, Oxfordshire OX11 0QX, U.K.;

Mónica Jiménez-Ruiz - Institut Laue-Langevin, 38042 Grenoble, France;

Stéphane Rols - Institut Laue-Langevin, 38042 Grenoble, France;

Agnieszka Poulain – University of Grenoble Alpes, University of Savoie Mont Blanc, CNRS, IRD, IFSTTAR, ISTerre, 38000 Grenoble;

Rogier Besselink – University of Grenoble Alpes, University of Savoie Mont Blanc, CNRS, IRD, IFSTTAR, ISTerre, 38000 Grenoble;

Stéphane Gaboreau – BRGM, Orléans Cedex 2 F-45060, France;

Sylvain Grangeon – BRGM, Orléans Cedex 2 F-45060, France;

Francis Claret – BRGM, Orléans Cedex 2 F-45060, France;

1 ABSTRACT

Calcium silicate hydrate (C-S-H) is a disordered, nanocrystalline material acting as the primary binding phase in Portland cement. Thin films of water are present on the surfaces and inside the nanopores of C-S-H and related phases such as calcium-aluminum-silicate-hydrate (C-A-S-H), an Al-bearing substitute present in low-CO₂ C-S-H cement. These water films control many of the chemical and mechanical properties of C-S-H, including drying shrinkage, ion transport, creep, and thermal behavior. Therefore, obtaining a fundamental understanding of their properties is essential. In this work, we have applied a combination of inelastic incoherent neutron scattering and molecular dynamics simulation methods to unravel the dynamics of water in synthetic C-(A)-S-H samples conditioned at five hydration states (from dry to fully hydrated) and with three different Ca/Si ratios (0.9, 1, and 1.3). Our results converge towards a picture where the evolution from thin layers of adsorbed water to bulk capillary water is dampened by the structure of C-(A)-S-H, in particular by the availability of Ca²⁺ sites which tend to keep the water in the form of structured surface layers.

2 INTRODUCTION

Cement paste is a multiphase material containing an extensive network of pores of different sizes. Water, either in bulk form or adsorbed at the surfaces of the different cement phases, is omnipresent.¹ The most important phase in cement is calcium-silicate-hydrate (C-S-H) and its Al-bearing analog, present in low-CO₂ cement calcium-aluminum-silicate-hydrate (C-A-S-H). The C-(A)-S-H phase itself is a nanocrystalline and disordered material with varying Ca/Si ratio and water content and distribution. Not surprisingly, water plays a crucial role as it directly influences the mechanical properties of cement, such as shrinkage, creep, and strength of concrete structures,² and fluid and solute transport processes that control cement geochemical alteration and durability.³ The detailed properties of cement pore water, however, remain challenging to characterize because of the complex, heterogeneous, and nanoporous structure of the material⁴⁻⁶. Hence, understanding water dynamics in cement systems remains a fundamental topic of interest⁷⁻¹¹.

Previous experimental studies of the dynamics of water have mostly focused on the entire cement paste, using different spectroscopic techniques that access different energy and spatial domains.

For example, Nuclear Magnetic Resonance provides information about the types of water, by probing the local environment of the proton, and about its relaxation and exchange dynamics.^{6,9,10,12–14} Infra-red and Raman spectroscopies are sensitive to the stretching and bending vibrational modes of water, yielding information about the local environment of water.^{7,15} Broadband Dielectric Spectroscopy accesses water motion regimes in different sized pores by probing its dielectric properties.^{1,16}

Inelastic neutron scattering (INS)^{3,17–19} and Quasielastic Neutron Scattering (QENS)^{3,19–21} also have been widely applied to probe the dynamics of water in cementitious materials and other confined water systems ranging from Vycor glass,²² to chalk,²³ silica glass,²⁴ and clay minerals.²⁵ These methods probe time domains from nano- to picoseconds and spatial domains from 0.1 to 10 nm, thus allowing the study of water rotational and translational dynamics (diffusion, exchange between different environments at interfaces and in nanopores). INS experiments performed on cement pastes under varying relative humidity (RH) conditions have been found to distinguish interfacial/interlayer water,^{3,19} translations of water molecules,^{26,27} translational dynamics of portlandite hydroxyl ions,^{17,18} and librational modes of water (H-bond hindered translations and rotations of water molecules).

Atomistic simulation methods, including notably molecular dynamics (MD)^{28–30} simulations, similarly can probe the dynamics of water in confined systems over time scales of nano to femtoseconds and length scales of 0.1 to 10 nm, allowing direct comparisons with experimental results from ¹H NMR, INS, QENS, and other experimental techniques. For example, a classical MD study by Kalinichev et al.³¹ revealed diffusion coefficients of $5.0 \times 10^{-11} \text{ m}^2/\text{s}$ for water in the tobermorite (a natural crystalline analog of C-S-H³²) and $6.0 \times 10^{-10} \text{ m}^2/\text{s}$ for water on the external interfaces, in agreement with QENS experimental results.^{12,33}

Experimental and computational studies using the methods outlined above have converged towards an identification of three water populations in cement paste with different dynamical properties: (i) bulk-like water that is weakly bound and evaporates at around 100°C, which is found in so-called gel pores larger than 3 nm in diameter; (ii) multilayer interfacial water found within 1 nm (~3 water layers) from the C-(A)-S-H surfaces and; (iii) chemically bound water that includes interlayer and strongly bound interfacial water and hydroxyls of Si-OH and Ca-OH groups. A characteristic of these studies is that they have been performed on cement pastes^{34,35} and many date back 10 to 20 years when limited instrumental resolution obstructed a detailed data interpretation^{17,19,21,36}. These studies were instrumental in revealing the complexity of C-(A)-S-H systems, including variability in the abundance of different phases and different water populations. However, their use of comparatively ‘macroscopic’ approaches in sample preparation has proved limiting in establishing a detailed molecular level understanding of water

in the pores or on the surfaces of the C-(A)-S-H phase of cement. In short, new mechanistic understanding of the role that water plays in cement phase requires approaches that can isolate water dynamics in the C-(A)-S-H phase.

In this work, we present an Inelastic Incoherent Neutron Scattering (IINS) investigation of water in hydrated synthetic C-(A)-S-H complemented with MD simulations of water dynamics in the same system using our recently developed C-S-H model.³⁷ IINS is a vibrational spectroscopic method that is extremely sensitive to hydrogen atom vibrations due to the very large incoherent scattering cross section of the H atom compared to other atoms. Consequently, it is ideal for studying water dynamics, providing access to a wide range of water vibrational modes across the spectroscopic spectrum. The IINS method offers several advantages compared to traditional spectroscopic techniques like Raman and IR spectroscopy: i) Due to the interaction of neutrons with the nuclei, no selection rules apply, enabling access to all vibrational modes involving H; ii) Neutron scattering methods are non-destructive, preserving the integrity of the sample for further analysis; and iii) Experimental neutron spectroscopy data can be readily complemented and interpreted by atomistic level simulations, including MD simulations.

We carried out IINS experiment, for C-(A)-S-H at three Ca/Si ratios (0.9, 1, and 1.3) and five hydration states (fully hydrated, oven-dried, conditioned at 55% and 98% RH levels, and desorbed/dried at 11% RH). First, we examine the impact of varying Ca/Si ratios and RH levels on our experimental IINS data. This analysis sheds light on how these factors influence the water dynamics within the C-(A)-S-H structure. Next, we utilize the generalized density of states (GDOS) predicted by MD simulations to deepen our interpretation of our experimental data and reveal the complex interplay between structural parameters and observed spectral features. Finally, we evaluate the diffusion coefficients of interfacial and interlayer water and subsequently compare them to the diffusion constant of bulk water. This comparison provides insights into the differing mobility behaviors of water in distinct compartments within the C-(A)-S-H system.

3 MATERIALS AND METHODS

3.1 Sample preparation

C-S-H samples of Ca/Si = 1, 1.2, and 1.3 were synthesized by reacting calcium oxide and fumed silica in water inside an N₂ wet glove box. Calcium oxide was obtained by calcination of CaCO₃ (Sigma-Aldrich, Fluka, Bioultra) at 1000 °C for 18 h and stored in a vacuum desiccator until usage. Fumed silica SiO₂ (Sigma-Aldrich, Aerosil 200) was placed in an oven at 40 °C for ~24 h to remove physisorbed water prior to each experiment. Deionized water was boiled and degassed with N₂ gas to remove all dissolved CO₂. The quantities of calcium oxide and fumed silica required to

prepare C-S-H of predetermined stoichiometry were calculated using the method reported by Haas and Nonat³⁸ (Table S1 in the Supporting Information). Samples were left reacting under stirring conditions for ~1 month in High Density Polyethylene (HDPE) bottles inside a wet N₂ glove box, then filtered using Millipore® filter paper (0.22 µm, GSW1 UM), and the wet C-S-H residue was left to dry inside a glove-box for ~12 h. The C-A-S-H samples with Ca/Si = 0.9, and Al/Si = 0.1, were synthesized following the protocol that can be found elsewhere³⁹. We use C-(A)-S-H when we refer both to C-S-H and C-A-S-H samples. Aliquots of these C-(A)-S-H samples were preserved and will be referred to as fully-hydrated or 'FH' C-(A)-S-H.

The remaining portion of each FH C-(A)-S-H sample was oven-dried at 40 °C in a vacuum oven for ~24 h. Based on previous studies⁷ and our own experience, this temperature is not sufficient to remove highly-bound water even under conditions of dynamic vacuum, but it is enough to evaporate the majority of bulk capillary-pore and adsorbed gel-pore water. A part of these samples was stored separately and is referred to as oven-dried or 'OD' C-(A)-S-H.

The remainder of each sample was exposed to a controlled RH of 55% or 98% using saturated salt solutions of Mg(NO₃)₂·6H₂O and K₂SO₄, respectively (Figure S1 in the Supporting Information). The equilibration times for C-S-H samples lasted 1 week, and for C-A-S-H samples 1 month. The different equilibration times were due to the availability of the neutron beamtime. We note that, ideally experiments involving water adsorption in C-(A)-S-H should be done in the same timeframe to eliminate the equilibration time effect. We refer to these C-(A)-S-H as '55RH' and '98RH' samples. Finally, a portion of each 98RH C-(A)-S-H sample was stored inside a vacuum desiccator containing silica beads to remove any adsorbed or bulk water⁴⁰. We named these samples desiccator-dried or 'DD' samples.

Following these conditioning protocols, we obtained C-S-H samples labeled CSH_Ca/Si_%RH, where %RH is the relative humidity value at which they were conditioned. The C-A-S-H samples were labeled CASH_Ca/Si_%RH. In the text, we refer to 'wet' (FH, 98RH) and 'dry' (55RH, OD, DD) C-(A)-S-H samples. As C-(A)-S-H is sensitive to atmospheric CO₂, all synthesis and conditioning processes were performed under an inert gas atmosphere of N₂.

3.2 Sample characterization

Inductively coupled plasma - atomic emission spectrometry (ICP-AES).

Ca/Si ratios were determined using ICP-AES (Varian 720ES Agilent). The C-(A)-S-H particles (5-10 mg) were dissolved by adding of concentrated 14 M HNO₃ (distilled) and 28 M HF (47-51%, Trace Metal™, for Trace Metal Analysis, Fisher Chemical) acids, followed by heating the solution for ~24h at ~80°C. The final step involved diluting with boric acid and ultrapure water up to 150 mL prior to the measurement.

Water adsorption volumetry

Water adsorption isotherms were obtained at 25 °C using a Belsorp-Max instrument by BEL JAPAN Inc. A long acquisition time of at least 2 weeks was required due to the slow equilibrium kinetics. Prior to the measurements, all samples were outgassed at 50 °C for 24 h under a residual pressure of 4.652×10^{-5} Pa. The classical Brunauer–Emmett–Teller (BET) theory was used to analyze the isotherms and derive the specific surface area (SSA)⁴¹ (Table 1).

Thermogravimetric analysis

Thermogravimetric analysis (TGA, Mettler-Toledo TGA-DSC3+) was used to examine the thermal decomposition and determine the water content of the C-(A)-S-H samples. The samples were analyzed at a heating rate of 10°C/min up to 600°C in an N₂ environment with a flow rate of 20 mL/min. The samples were loaded in aluminum crucibles and were hermetically sealed with aluminum caps inside a glove box or a glove bag filled with N₂ equilibrated at the same RH used to condition the sample. The sample mass used for TGA analyses varied between 8 and 30 mg. The amounts of water deduced from the TGA have been normalized per mass of C-S-H measured at the end of the heating, at 600°C.

Synchrotron X-Ray diffraction

Synchrotron XRD measurements for the C-S-H samples were performed at the ID31 beamline of the European Synchrotron Radiation Facility (ESRF) in Grenoble, France. Prior to analysis, C-(A)-S-H samples were loaded into 1.5 mm (ID31) polyimide capillaries inside the glove bags, or wet glove-box, at the same RH values. The capillaries were sealed airtight on both ends using a two-part epoxy adhesive.

At the ID31 beamline, a monochromatic X-ray beam of 78 keV ($\lambda = 0.159$ Å) was used to obtain scattering patterns of C-S-H samples. The data sets were collected using a PilatusX 2M CdTe detector placed at a sample-to-detector distance of $d_1 = 1.226$ m to obtain scattering patterns with a Q range of 0.1–6.2 Å⁻¹. This allowed the measurement of the Bragg peak corresponding to the interlayer distance of C-S-H. Data were automatically corrected for internal dark current. Two-dimensional images of the scattered intensity were azimuthally integrated using the pyFAI software package⁴². The pattern from the empty capillary was subtracted as a background.

The C-A-S-H samples were measured at the 11-ID-B beamline at the Advanced Photon Source, Argonne National Laboratory. Samples were analyzed with a monochromatic X-ray beam of 58.6 keV ($\lambda = 0.2115$ Å). Data were collected with a Perkin Elmer XRD 1621 N ES detector and sample-to-detector distance of $d = 0.799$ m to access a Q range of 0.2–10.4 Å⁻¹. Data were automatically corrected for internal dark current. Two-dimensional images of the scattered intensity were azimuthally integrated using the GSAS II software package⁴³.

Distribution of water in C-(A)-S-H

The total weight loss (from 25 to 600°C) qualified by TGA, which includes all water and hydroxyls in the samples, is referred to here as ‘total water’ amount. We opted to include the hydroxyl groups in the total mass, because in the IINS experiment we cannot separate the signals from water and hydroxyls. The amount of bulk-like water is quantified based on the first minimum of each dTG curve around 100°C (Figure S3 in the Supporting Information). We note that this water classification is based on the energetics of water release from C-(A)-S-H. Thus, bulk-like water is water that evaporates at around 100°C and is found predominantly in large gel pores (>3 nm), but small amounts of bulk-like water are also found in the ‘dry’ samples as remnant water inside the large pores. The amount of non-evaporable interlayer and strongly bound monolayer water was assumed to be the water in OD samples after the bulk-like water is evaporated. This value was called “Interlayer, hydroxyl, and monolayer water” in Table 1 and was the same for all samples for a given Ca/Si with a total weight larger than the OD sample. This assumption is valid because the OD sample was the starting sample that was subjected to wetting (see sample preparation Figure S1).

The amount of multilayer adsorbed water upon rewetting was calculated by subtracting the bulk-like water, interlayer, and monolayer water from the total water amount. Within this category, the amount of water that entered the interlayers and led to swelling of the interlayer space (as evidenced by increasing XRD d_{001} values) was named the ‘Multilayer and interlayer water’.

3.3 Inelastic Incoherent Neutron Scattering

The inelastic neutron scattering event involves both energy (E , cm^{-1}) and momentum ($|Q|$, \AA^{-1}) transfer. The energy transfer (E_T) is defined as $E_T = E_i - E_f$ where i and f refer to the incident and final values, respectively. The momentum transfer is given by $\mathbf{Q} = \mathbf{k}_i - \mathbf{k}_f$, where the absolute value of the wavevector \mathbf{k} is defined as $|\mathbf{k}| = \frac{2\pi}{\lambda}$, and λ is the wavelength of the neutron. IINS captures vibrational modes across the wide energy range, from the microwave to the ultraviolet regions. We are most interested in the region spanning from microwave to mid-infrared, i.e., from 20 to 2000 cm^{-1} .

INS spectra of C-S-H samples with Ca/Si = 1.2 and 1.3 were collected in the energy range from 133.3 to 1940 cm^{-1} (16.5 to 240 meV) with an energy resolution of $\Delta E/E \sim 2\text{-}3\%$ using the Lagrange (LArge GRaphite ANalyser for Genuine Excitations) secondary spectrometer at the hot source of high-flux reactor of the Institut Laue-Langevin (ILL), France^{44,45}. A combination of two double focusing monochromators was used to access the energy range: Cu(220) to access the intermediate energies, and Si(311) for lower energies.

The energy transfer range was obtained by subtracting the final energy of 4.5 meV of PolyGraphite (PG) analyzers from the experimentally obtained one. The samples were loaded into hollow aluminium cells, which were sealed under RH conditions matching the preparation of each of C-S-H samples. The INS spectra were collected at 10 K (to lower the Debye-Waller factor) for the samples, the empty holders, and the cryostat. The background spectrum from the latter was subtracted from the raw INS spectra of the C-S-H samples. The obtained intensity was normalized by the monitor counts using LAMP (Large Array Manipulation Program) software.⁴⁶

The $S(\mathbf{Q}, \omega)$ from Cu(220) and Si(311) reflecting planes were manually merged to obtain the final $S(\mathbf{Q}, \omega)$ in the range 133.3 to 1940 cm^{-1} . Providing that the final wavevector, k_f , is much smaller than the incident wavevector k_i , the observed intensity is directly proportional to the generalized density of states (GDOS), which in the case of hydrogenated samples is the hydrogen partial density of states.

The INS spectra of C-S-H samples with Ca/Si = 1, and C-A-S-H samples with Ca/Si = 0.9 were measured at 10 K using TOSCA spectrometer at the ISIS spallation Neutron and Muon Source (Rutherford Appleton Laboratory, UK).^{47,48} TOSCA is an indirect geometry time-of-flight spectrometer operating in the energy transfer ranges up to 8000 cm^{-1} with an $\Delta E/E$ resolution of $\sim 1.25\%$. The samples were loaded in Al cells and sealed with In-wire under RH conditions matching the preparation of the C-S-H samples. All manipulations were performed inside a wet glove box or glove bags to prevent contamination by carbon dioxide. The Al cells were then mounted on a center stick connected to a gas handling system. The INS signals from sample scattered neutrons and empty Al cells were recorded by detectors both in forward and in backward directions for about 4 hours per sample. The neutron beam size was approximately 40 mm x 40 mm. The resulting data were combined using Mantid software.⁴⁹ Inelastic signals coming from the empty Al cells were subtracted for each sample, and the spectra were scaled by sample mass. More precisely, spectra were normalized by initial sample mass, i.e., the mass of the oven-dried C-S-H samples before conditioning at varying RH levels.

3.4 Molecular Dynamics Simulations

Atomistic simulations were performed at the Cori supercomputer at the National Energy Research Scientific Computing Center (NERSC, USA) using the MD simulation code LAMMPS,⁵⁰ which solves Newton's equations of motion for many-particle systems interacting through pairwise potentials. Interatomic interactions were described using the SPC water model,⁵¹ and the CLAYFF model of mineral-water interactions.^{52,53} The CLAYFF force field was chosen because of its versatility and successful descriptions of various systems including clay minerals,^{31,54–57} zeolites,⁵⁸ and other phases,^{59–61} validated against the results of X-ray and neutron scattering experiments,^{31,62} and a variety of other experimental techniques.^{63,64}

The structure of the C-S-H nanoparticle model is described in detail elsewhere³⁷ and is briefly presented in Figure S2 in the Supporting Information. While we acknowledge the existence of the C-S-H sheet model,⁶⁵ for the purposes of this discussion whether the edges of the C-S-H particle are chemically connected or not should have little or no impact on our results. The C-S-H model used in our MD simulations is based on the colloidal model by Jennings,⁶⁶ and it describes well the structural characteristics of interfacial water³⁷.

We have simulated our C-S-H nanoparticle model at two hydration states: a comparatively 'dry'-state named 'CSH-dry-NP' with $\text{H}_2\text{O}/\text{Si} = 1.35$ (molecules/molecules) and interlayer spacing $d_{001-\text{MD}} = 11.0(2) \text{ \AA}$ and a fully hydrated state 'CSH-wet-NP' with $\text{H}_2\text{O}/\text{Si} = 38.5$ and interlayer spacing $d_{001-\text{MD}} = 13.0(2) \text{ \AA}$.³⁷ Analyses of the MD simulation trajectories were performed using custom-made Python codes over the frames from the production runs. The GDOS of the two simulated systems were calculated using the Molecular Dynamics Analysis for Neutron Scattering Experiments (MDANSE) python-based application.⁶⁷

4 RESULTS AND DISCUSSION

4.1. Water content in C-(A)-S-H samples as a function of Ca/Si

Calcium-(aluminium)-silicate-hydrates are well known to have varying stoichiometry depending on the Ca/Si ratio, the hydration state of the sample, and the abundance of defects in the C-(A)-S-H structure.⁶⁸⁻⁷⁰ To discern this variations, we determined the water content and distribution in our C-(A)-S-H samples at three Ca/Si ratios (0.9, 1, and 1.3), encompassing five different hydration states and an additional sample of CSH_1.2_DD.

'Dry' C-(A)-S-H samples (55RH, OD and DD)

Results from the TGA experiments indicate similar amounts of water for all 'dry' C-(A)-S-H samples. The total amount of water in 'dry' C-(A)-S-H were constant regardless of Ca/Si value and in accordance with the literature⁷¹. The average quantity of total water for OD samples was about 18 wt.%. The d_{001} spacing values for OD samples were about 0.6 \AA lower than for DD samples, which can be explained by the more efficient removal of interlayer water under vacuum.

The 55RH C-(A)-S-H samples contained about 20 wt.% of total water irrespective of Ca/Si ratios. We calculated the amount of water adsorbed upon rewetting at 55% RH by subtracting the 'interlayer, hydroxyl, monolayer' and bulk-like water from the total water. The results of TGA and WSI point to decreased amounts of adsorbed water with increasing Ca/Si ratios. The WSI results show that the amount of adsorbed water for CASH_0.9 was roughly 1.9 times larger than for CSH_1.3 and CSH_1 (Table 1).

Exposure of the 98RH samples to a desiccator environment (<11% RH) containing silica gel led to a reduction in total water content by 10-20 wt.% and to the transformation of these samples

into DD samples. TGA and dTG curves reveal that 98RH samples lost primarily bulk-like capillary pore water and adsorbed gel pore water, resulting in ~16 wt.% of total water in DD samples (Figure S3 in the Supporting Information). At RH levels <11%, ‘drying’ of the interlayer also takes place^{4,40,72}, leading to a contraction of the d_{001} values, observed through XRD (Figure 1). The extent of C-(A)-S-H interlayer space contraction is about 2.5 Å, on average, from ‘wet’ to ‘dry’ samples, consistent with the work of other researchers (who reported ~3 Å)⁷. This value is roughly the size of a water molecule, which is complementary to the TGA data showing a difference of about 1 H₂O/Si between the ‘dry’ and ‘wet’ C-(A)-S-H samples also reported in the literature^{7,70,71}.

Table 1. Summary of TGA, WSI, and XRD results for ‘wet’ and ‘dry’ C-(A)-S-H samples. Columns 3-6 refer to TGA results in units of mmol/g_{CSH-dry} (mass of C-(A)-S-H samples at 600 °C, at the end of the TGA cycle). Column 7 refers to WSI results in units of mmol/g_{CSH-dry} (mass of C-(A)-S-H samples after the WSI pre-treatment with 50 °C in the vacuum).

| Sample name | Total water, wt.% (25-600°C) | Bulk-like water (100°C) | Interlayer, hydroxyl & monolayer water | Multilayer & interlayer water | WSI adsorbed water | SSA (m ² /g) | d_{001} -XRD (Å) |
|---------------------------|------------------------------|-------------------------|--|-------------------------------|--------------------|-------------------------|--------------------|
| C-A-S-H. Ca/Si=0.9 | | | | | | | |
| DD | 16±2 | 2±0.7 | 8.6±0.7 | | | 353 | 12(2) |
| OD | 19±2 | 4.2±0.7 | 9.4±0.7 | | | | 11.9(2) |
| 55RH | 22±2 | 4.6±0.7 | 9.4±0.7 | 0.5±0.9 | 8.35 | | 12.4(2) |
| 98RH | 36±2 | 11.3±0.7 | 9.4±0.7 | 11.1±0.9 | 22.25 | | 13.7(2) |
| C-S-H. Ca/Si=1 | | | | | | | |
| DD | 15±2 | 0.8±0.7 | 9.2±0.7 | | | 180 | 11.6(2) |
| OD | 17±2 | 0.8±0.7 | 10.3±0.7 | | | | 10.6(2) |
| 55RH | 23±2 | 2.5±0.7 | 10.3±0.7 | 4.1±0.9 | 4.43 | | 12(2) |
| 98RH | 27±2 | 5.2±0.7 | 10.3±0.7 | 4.9±0.9(2) | 20.31 | | 12.3(2) |
| FH | 28±2 | 6.1±0.7 | 10.3±0.7 | 5.2±0.9 | 0 | | 13.1(2) |
| C-S-H. Ca/Si=1.3 | | | | | | | |
| DD | 16±2 | 1±0.7 | 9.2±0.7 | | | 135 | 10.4(2) |
| OD | 17±2 | 1.6±0.7 | 9.8±0.7 | | | | 9.8(2) |
| 55RH | 20±2 | 1.6±0.7 | 9.8±0.7 | 2.3±0.9 | 4.38 | | |
| 98RH | 24±2 | 2.7±0.7 | 9.8±0.7 | 4.4±0.9 | 14.11 | | 11.9(2) |
| FH | 26±2 | 5±0.7 | 9.8±0.7 | 5.2±0.9 | | | 11.5(2) |
| C-S-H. Ca/Si=1.2 | | | | | | | |
| DD | 16±2 | 0.9±0.7 | 9.5±0.7 | | | 177 | 10.6(2) |

‘Wet’ C-(A)-S-H samples (FH and 98RH)

The TGA results revealed that fully-hydrated samples CSH_1_FH and CSH_1.3_FH contain 28, and 27 wt.% of total water, respectively. This total water consists primarily (mol/g_{dry-CSH}) of less strongly bound bulk-like capillary water, as indicated by intense dTG minima centered at 100°C

(Figure S3 in the Supporting Information). The FH samples have interlayers filled with water molecules, reflected in d_{001} values of 11.5 Å for CSH_1.3 and 13.1 Å for CSH_1 sample. These values are about 2 to 2.5 Å larger than for 'dry' C-(A)-S-H samples (Table 1).

WSI was used to calculate the specific surface areas of C-(A)-S-H accessible to water. According to the IUPAC classification⁷³, the water sorption isotherms belong to type II with an H3 hysteresis type formed throughout the whole RH range (Figure 1). A characteristic hysteresis between adsorption and desorption branches, and a sudden drop in the adsorbed amount at RH ~35% were observed for nearly all samples. The origin of the hysteresis is generally explained by the presence of 'ink bottle pores' that have narrow entrances to the pore, which are considerably smaller than the actual pore diameter⁷⁴. The BET method⁴¹ allows the calculation of the SSA from the adsorption branch at relative pressure levels from 0.05 to 0.3. The results show a clear decrease in SSA of C-(A)-S-H at increasing Ca/Si ratios (Table 1). For Ca/Si ratios from 0.9 to 1.3, the SSA decreases from 353 m²/g for CASH_0.9 to 135 m²/g for CSH_1.3. We note that the absolute values for surface areas of cement pastes and pure C-S-H vary widely depending on the adsorbate used, the drying technique, and the temperature of the sample^{74,75}.

The rewetting at 98% RH of the OD (oven-dried) samples proceeds through water populating the interfaces and the interlayer⁴⁰, with the amount of adsorbed water depending on the equilibration time⁷⁶. The comparison of our WSI data with the data from Roosz et al.⁸ show that long exposure to RH > 95% leads to higher amounts of water being adsorbed on the C-(A)-S-H surfaces, followed by capillary condensation in pores. This phenomenon results in varying amounts of total water for 98RH C-(A)-S-H samples at varying Ca/Si ratios.

We calculated the amount of adsorbed water in our C-(A)-S-H samples by subtracting the 'Interlayer, hydroxyl, and monolayer' and bulk-like water from the total water amounts in our 98RH samples. Some part of this adsorbed water condenses in large gel pores and stays as bulk-like water. The TGA/dTG curves show that the proportions of bulk-like water to total water decrease from CASH_0.9 to CSH_1 to CSH_1.3. Some part of the adsorbed water stays as multilayer interfacial water, and some water enters the interlayers thus increasing d_{001} reflection values by 1.8 to 2 Å (Table 1).

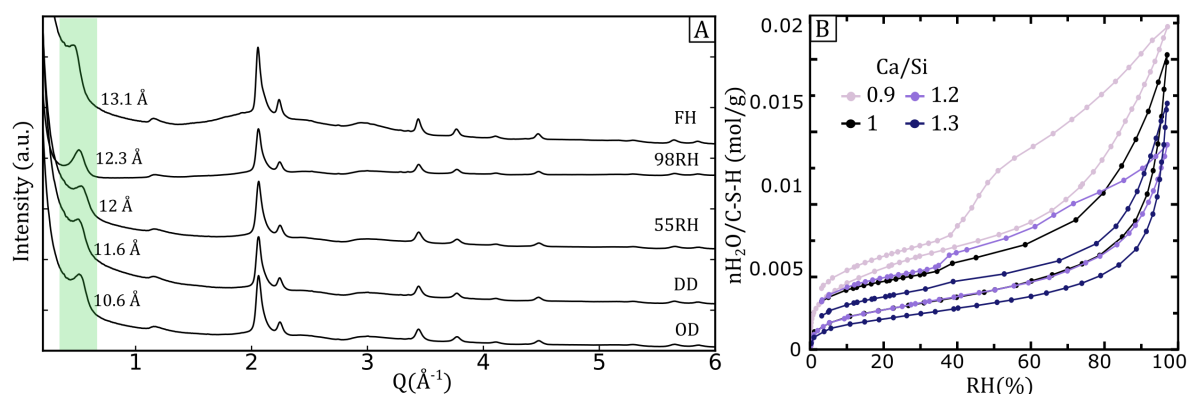


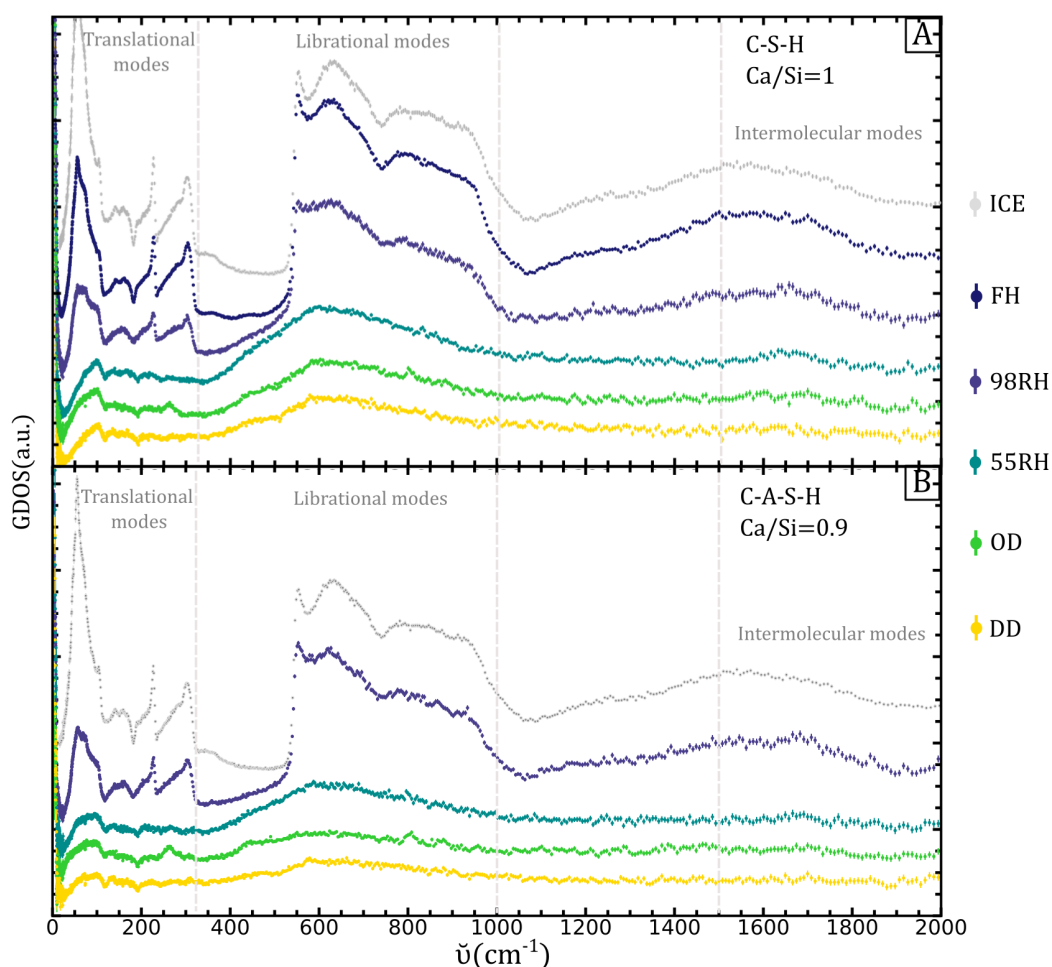
Figure 1. (A) X-ray diffraction patterns of CSH_1 sample showing changes in the d_{001} values with changing RH levels: FH (fully hydrated), 98RH (conditioned under 98% RH), 55RH (conditioned under 55% RH), DD (desiccator dried), OD (oven dried); (B) Water sorption isotherms of C-(A)-S-H samples showing the amounts of adsorbed water at increasing RH values.

4.2. Experimental IINS data

In this section we detail the results of the IINS experiments that were used to probe the dynamics of water in C-(A)-S-H samples with three Ca/Si ratios (0.9, 1, 1.3) at five hydration levels. The integrated intensity of the IINS spectra (GDOS) is proportional to the total amount of water and hydroxyls in the C-(A)-S-H samples.

4.2.1. Impact of RH level in CSH_1

A first comparison between the C-S-H and ice Ih spectra allow distinguishing the 'dry' C-S-H samples (green-yellow curves) from the 'wet' C-S-H samples (blue curves) (Fig. 2). The former contains only interlayer and interfacial water and have lower water content than the 'wet' samples (as deduced from WSI, TGA and XRD data). The spectra resulting from the 'wet' C-S-H samples contain bulk capillary pore water in addition to the interlayer and interfacial water.



369

370 *Figure 2. Evolution of the generalized density of states (GDOS) of (A) CSH_1 samples; (B) and CASH_0.9 samples*
 371 *with increasing hydration states. For the sake of clarity, all the spectra have been arbitrarily shifted along the*
 372 *GDOS axis. The spectra have been normalized to the water content of the sample in the beam. The translations*
 373 *of water molecules at 80, 226, and 305 cm⁻¹ (10, 28, and 38 meV) evident in samples containing bulk-like water*
 374 *(FH and 98RH) evolve into the dampened signal at 96 cm⁻¹ (12 meV) upon loss of water. Accordingly,*
 375 *librational edges evolve from the sharp vertical onset in FH samples into a rising slope in dry samples (55RH,*
 376 *OD, DD). The librational edges of 98RH samples contain features of bulk-like water and multilayer adsorbed*
 377 *water. Librational modes, which reflect the hydrogen bonding network, undergo changes in shape and*
 378 *intensity as they transition from an ice-like distribution to a broader triangular shaped distribution spanning*
 379 *a range of frequencies from 400 to 1000 cm⁻¹ (equivalent to 50 to 125 meV). The librational modes of drier*
 380 *samples (OD, DD) have lower intensities than the 55RH samples, reflecting their smaller water content and*
 381 *less extensive H-bonding network.*

382 The power spectra of ice Ih (grey curve in Figure 2) can be broken down into three different
 383 regions: a low energy part representing the translational modes at 0-323 cm⁻¹ (0-40 meV); a
 384 librational region, which represents hindered rotations of H-bonded water molecules, is found
 385 between 444-968 cm⁻¹ (55-120 meV); the high frequency intramolecular vibrations, such as
 386 bending modes are observed at 1613 cm⁻¹ (200 meV) and O-H stretching modes at 3307 cm⁻¹ (410
 387 meV)⁷⁷.

Lower energy modes (0-320 cm⁻¹)

The lower energy translational modes in ice Ih are characterized by the triangular features at 57 cm⁻¹ (~7 meV) known as acoustic modes, and at 226 and 298 cm⁻¹ (28 and 37 meV) known as optic modes. These modes involve the O-H stretch for a tetrahedral bonding motif in the ice lattice⁷⁸. The same translational modes are evident in the 'wet' C-S-H samples, with slightly lower relative intensities than in ice Ih. On the other hand, the 'dry' C-S-H samples show a dramatic change in the region of lower energies, with translational and acoustic modes attenuated and shifted to higher frequencies. This implies that the ordered structure coming from the H-bonding network is not present and means that the water is strongly bound to the C-S-H surfaces and that water molecules have a different local order than in ice Ih.

The behavior described above has been previously observed for water adsorbed at the solid-water interfaces of other nanosystems^{3,23,77,79-82}. In the case of cementitious materials, previous INS studies have identified the peaks at around 80 and 242 cm⁻¹ (10 and 30 meV) as 'fingerprints' of confined water. In computer simulations⁸³ and experimental studies on Vycor glasses^{22,26}, these peaks have been attributed to the translational motions of water molecules inside the confining cage. Analogous peaks are observed at about 97 and 249 cm⁻¹ (12 meV and 30.9 meV). The difference in peak position relative to previous studies of cementitious materials could be due to the improved resolution of the instruments or to the tendency of these peaks to shift and vary in spectral intensity depending on the ions present in the system and the hydration state^{82,84}. Finally, the temperature of the experiment affects the intensities of these peaks, with a significant sharpening of the signals as temperature goes below 0°C²². In our case, we have assigned these peaks to the dangling hydrogens of strongly bound interfacial water molecules, based on the calculated partial GDOS as will be explained later.

Librational modes (300-1000 cm⁻¹)

The librational modes found between ~300-1000 cm⁻¹ (37-124 meV) are very sensitive to the strength of the hydrogen bonds. The librational modes include the rocking, twisting, and wagging modes with their corresponding energies increasing accordingly (shown schematically in Figure S3 in the Supporting Information). However, the modes associated with different motions are strongly coupled and cannot be readily deconvolved^{84,85}. The librational edge represents the start of the librational modes energies, with a sharper edge at the low frequency side signaling the presence of a highly ordered structure with degeneration of some of these modes into a sharp peak indicative of water forming an extensive H-bonding network.

The evolution of the shift of the librational edge as a function of the water content can be followed by the changes observed from about 350 cm⁻¹ (~43.3 meV) for 'dry' to nearly 520 cm⁻¹ (~204 meV) for 'wet' C-S-H samples. The absence of a clear librational edge (a broken degeneracy of the

librational modes) similar to ice confirms the absence of bulk-like water in the 'dry' C-S-H samples. Among the 'dry' C-S-H samples, the librational modes of the OD and DD samples show shoulders at about 500 cm^{-1} (a convolution of the rocking, twisting, and wagging modes), while the 55RH C-S-H sample shows a smoother and sharper edge, indicating the presence of more water. This is in good agreement with the results of TGA, which show that CSH_1_55RH contains 35% and 41% more of total water than the OD and DD samples, respectively (Table 1). Experimental⁸ and computational⁸⁶ work has shown that at ~55% RH, C-S-H contains both interlayer and multilayer adsorbed water.

The 'wet' C-S-H samples reveal a close resemblance to ice, showing that they contain bulk liquid-like capillary pore water in addition to the interlayer and interfacial water. The CSH_1_98RH incorporates less bulk water than the fully hydrated C-S-H sample as shown by the results of the TGA and XRD experiments. Indeed, the start of the librational edge of CSH_1_98RH coincides with that of CSH_1_55RH, followed by a sharp vertical rise coinciding with the librational edge of ice Ih at around 500 cm^{-1} (62 meV) shown in Figure 2A. The 'combined' edge of CSH_1_98RH shows that the sample contains multilayer water, together with bulk capillary pore water. We performed the linear combination fitting by taking two end members (dFH and d55RH) to fit C-S-H_98RH samples. Both dFH and d55RH spectra are the results of the subtraction of OD from FH and 55RH spectra, respectively. The subtraction of the OD spectrum aimed to remove most of the contributions from interlayer and monolayer water, thus leaving predominantly bulk-liquid-like water in dFH and multilayer adsorbed water in d55RH spectra (Table 1). The CSH_1_98RH spectrum showed a good match to an evenly-weighted-sum of the dFH and d55RH spectra (Figure 3A). The fit results are in good accordance with the TGA data, showing that upon rewetting of the CSH_1 sample at 98% RH, the water distributed as 52% of bulk-liquid-like water and 48% multilayer adsorbed water.

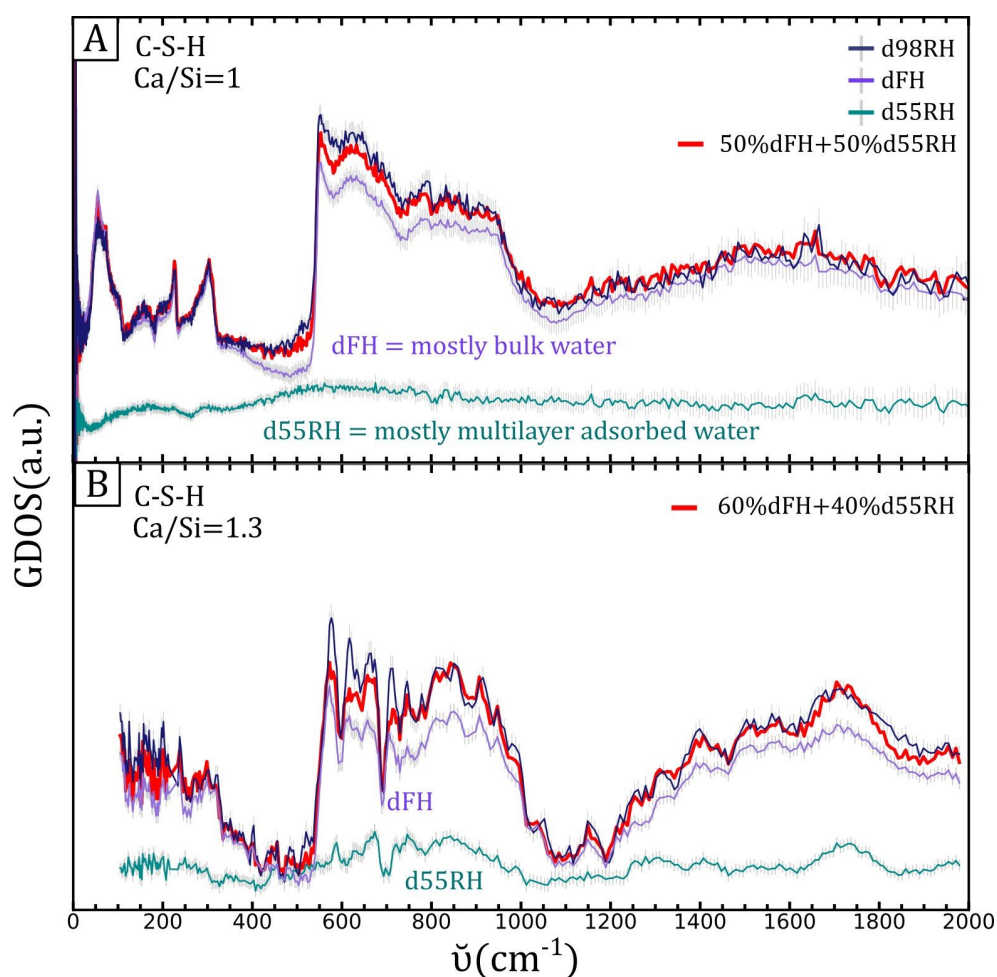


Figure 3. Linear combination fittings of C-S-H 98RH samples: (A) Ca/Si = 1 best fit with 50% of dFH and 50% of d55RH samples; (B) Ca/Si=1.3 best fit with 60% of dFH and 40% of d55RH samples.

Intermolecular modes (1500-4000 cm⁻¹)

At higher energies, we observe intermolecular modes including H-O-H bending modes at around 1650 cm⁻¹ (205 meV) and O-H stretching modes at around 3600 cm⁻¹ (446 meV). The values of the former and the latter modes tend to shift to higher frequencies with increasing water content. In our case, this is not observed because both bending and stretching modes are difficult to distinguish from the background signals. There are several plausible explanations: first, there is a Q dependence in IN1-Lagrange and TOSCA instruments where the data have been collected. The limited Q range of these instruments means that at higher energy transfers the resolution is dampened significantly. Secondly, the Debye-Waller effect i.e., the thermal fluctuations, at higher Q values substantially attenuate the intensity in the spectra. Experiments were performed at 10 K to avoid most of thermal fluctuations. Finally, at higher Q ranges there is an increase in multiphonon intensity, which gives a rising background with increasing Q values.

4.2.2. Impact of RH levels in CASH_0.9

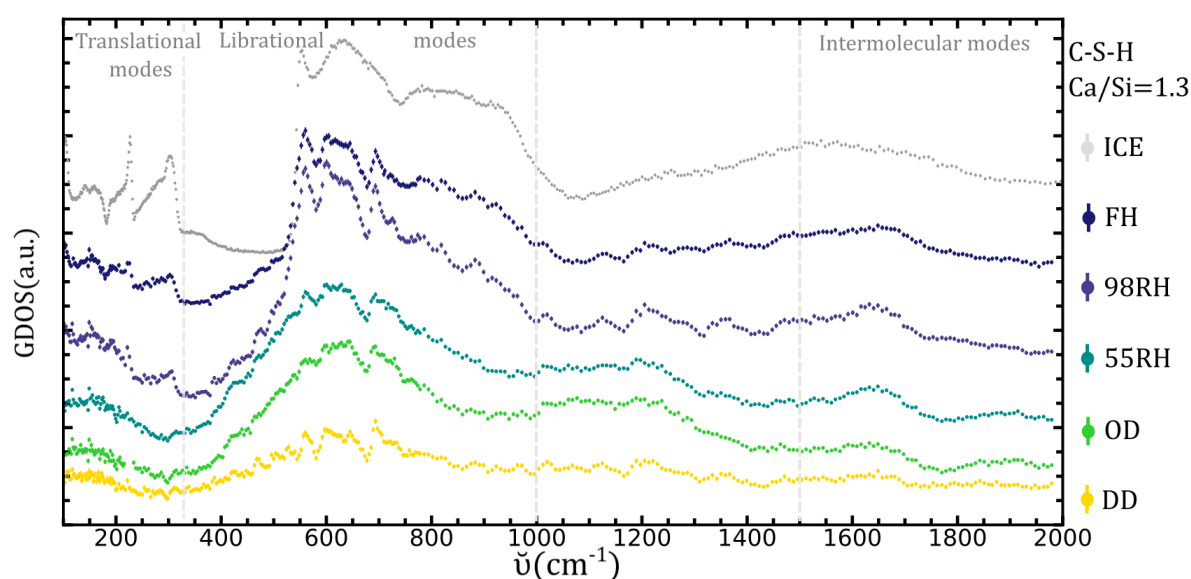
IINS spectra of CASH_0.9 with different water contents are shown in Figure 3. A detailed examination reveals a close resemblance to CSH_1. This behavior is expected, as in our samples the ratio of Al ions per Si is 0.1, and the effect of the Al is limited. However, some differences should be addressed.

First, similar to the CSH_1_98RH, the CASH_0.9_98RH contains multilayer water and some bulk pore water, as deduced from the librational edge, which could be decomposed as a linear combination of the signals from CASH_0.9_55H, and ice Ih edges. However, the relative intensities of the lower energy range translational modes (100-250 cm⁻¹, 15-40 meV) to the intensities of the librational modes are closer to those of ice Ih, than in CSH_1. This can be explained by the greater amount of water adsorbed at a given RH for CASH_0.9 than for the CSH_1 samples as shown by the results of WSI, TGA, and XRD (Table 1).

Secondly, the shape of CASH_0.9_98RH coincides with the shape of Ice Ih (Figure 2B), except for the absence of the characteristic dip in intensity at 350-550 cm⁻¹ (43.4-68 meV) and the lower intensities of the acoustic mode at 56.5 cm⁻¹ (7 meV). This reveals that multilayer water adsorption leads to capillary condensation of water in the larger gel pores and capillary pores with increasing RH. Another difference is in the acoustic mode peak which was damped and shifted in CSH_1 and is wider in the case of CASH_0.9, in line with our discussion about the changing value, shape, and intensity of this band.

4.2.3. Impact of RH level in CSH_1.3

The evolution of spectra for C-S-H with Ca/Si = 1.3 (CSH_1.3) as a function of RH is shown in Figure 4. The tendency towards the formation of an ice-like structure at increasing RH values is again observed. However, there are a few significant differences, which stem from the changing nature of C-S-H depending on the Ca/Si ratio.



487

488 *Figure 4. Evolution of the GDOS of CSH_1.3 samples with increasing hydration state. All the spectra have been*
 489 *normalized to the water content of the sample in the beam. For the sake of clarity, all the spectra have been*
 490 *arbitrarily shifted along the GDOS axis. The translations of water molecules at 226 and 305 cm⁻¹ (28 and 38*
 491 *meV) evident in samples containing bulk-like water (98RH) evolve into dampened signals upon loss of water.*
 492 *Additionally, the OV sample shows a peak at 260 cm⁻¹ (32 meV). Similar to CSH_1 and CSH_1.3 samples, the*
 493 *librational edges evolve from the sharp vertical onset in the ice into a rising slope in dry samples (55RH, OD,*
 494 *DD). The librational edges of FH and 98RH samples contain features of both bulk-like water and interfacial*
 495 *and interlayer water. The librational modes in the 55RH sample, which are indicative of the hydrogen bonding*
 496 *network, alter their shape and intensity as they transition from an ice-like distribution to a broader triangular*
 497 *distribution. This transition occurs in a frequency range from 400 to 1000 cm⁻¹ (corresponding to 50 to 125*
 498 *meV). These sets of spectra have been collected at IN1-Lagrange, ILL. The x-axis starts from 100 cm⁻¹ due to*
 499 *the experimental setup.*

500 The main differences are observed in the range of low energies for CSH_1.3 compared to CSH_1
 501 and CASH_0.9. The very different shape of spectra at lower energies comes from the peculiarities
 502 of the IN1-Lagrange instrument where the data were collected. The Q range for CSH_1.3 samples
 503 spans from 100-2000 cm⁻¹ (~15-250 meV), which is obtained by stitching the IN1-Lagrange data
 504 from the two monochromators manually. The acoustic signals at 226 and 298 cm⁻¹ (28 and 37
 505 meV) present in ice Ih exist also in CSH_1.3_FH, and with lesser intensities in CSH_1.3_98RH
 506 samples.

507 The 'wet' CSH_1.3 samples show fewer ice-like features than C-S-H_1 samples for a given RH. We
 508 also performed a linear combination fitting for the CSH_1.3_98RH sample and found a good fit
 509 with 60% of dFH and 40% of d55RH samples (Figure 3B), comparable to the TGA data. The TGA
 510 data shows that water adsorbed upon rewetting of CSH_1.3 sample at 98% RH consists of 38%
 511 bulk-liquid-like water, which evaporates at 114°C, and of 62% multilayer adsorbed water.

512 The difference between CSH_1, CASH_0.9, and CSH_1.3 samples can be explained based on three
 513 factors: (i) C-S-H samples tend to adsorb less water at a given RH with increasing Ca/Si ratios.

This observation is supported by the results of WSI, which show that the amount of adsorbed water at 98% RH is 1.1 times higher for CASH_0.9 than for CSH_1 and 1.6 times higher than for CSH_1.3 (Table 1). (ii) A high number of Ca^{2+} sites in the sample implies a higher proportion of Ca-hydration water, which is highly structured (i.e., non-bulk water). Our MD simulations, as well as others⁸⁷, showed that Ca^{2+} ions act as hydrophilic centers creating hydration shells and induce a H-bonding network. Therefore, a higher density of calcium ions in CSH_1.3 results in a greater proportion of bound water and a smaller proportion of bulk-liquid-like water. (iii) We note that the amount of adsorbed water on C-(A)-S-H surfaces is highly dependent on the equilibration time^{88,89}. In our case, the CASH_0.9 sample was equilibrated under 98% RH conditions 4 times longer than the C-S-H samples (1 month vs. 1 week). Therefore, the larger amount of adsorbed water can be explained partially by a lengthier exposure to a high humidity atmosphere.

Overall, the shapes of the librational modes can be used to differentiate between adsorbed interfacial water and bulk pore ice-like water in all C-(A)-S-H samples. For all C-(A)-S-H samples equilibrated at higher RH levels we observed a very close resemblance to ice Ih due to the presence of bulk-liquid-like pore water, whereas at lower RH levels typical confined water signals were present at lower energies of confined water were present in CSH_1 and CASH_0.9 samples.

4.2.4. Amount and distribution of water as a function of Ca/Si ratio

In Figure 5, we highlight differences in the IINS spectra arising from changing Ca/Si ratio in ‘wet’ and ‘dry’ C-(A)-S-H samples. We note that we simultaneously examine the *amount* and *distribution* of adsorbed water since IINS allows observing directly both of these characteristics. There is a direct dependence between an increased amount of water and an enhanced spectral intensity. At the same time, the type of water affects the overall shape (and to some extent the intensity) of the spectra. The two types of water that IINS allows us to distinguish are interfacial and interlayer water versus bulk-liquid-like water.

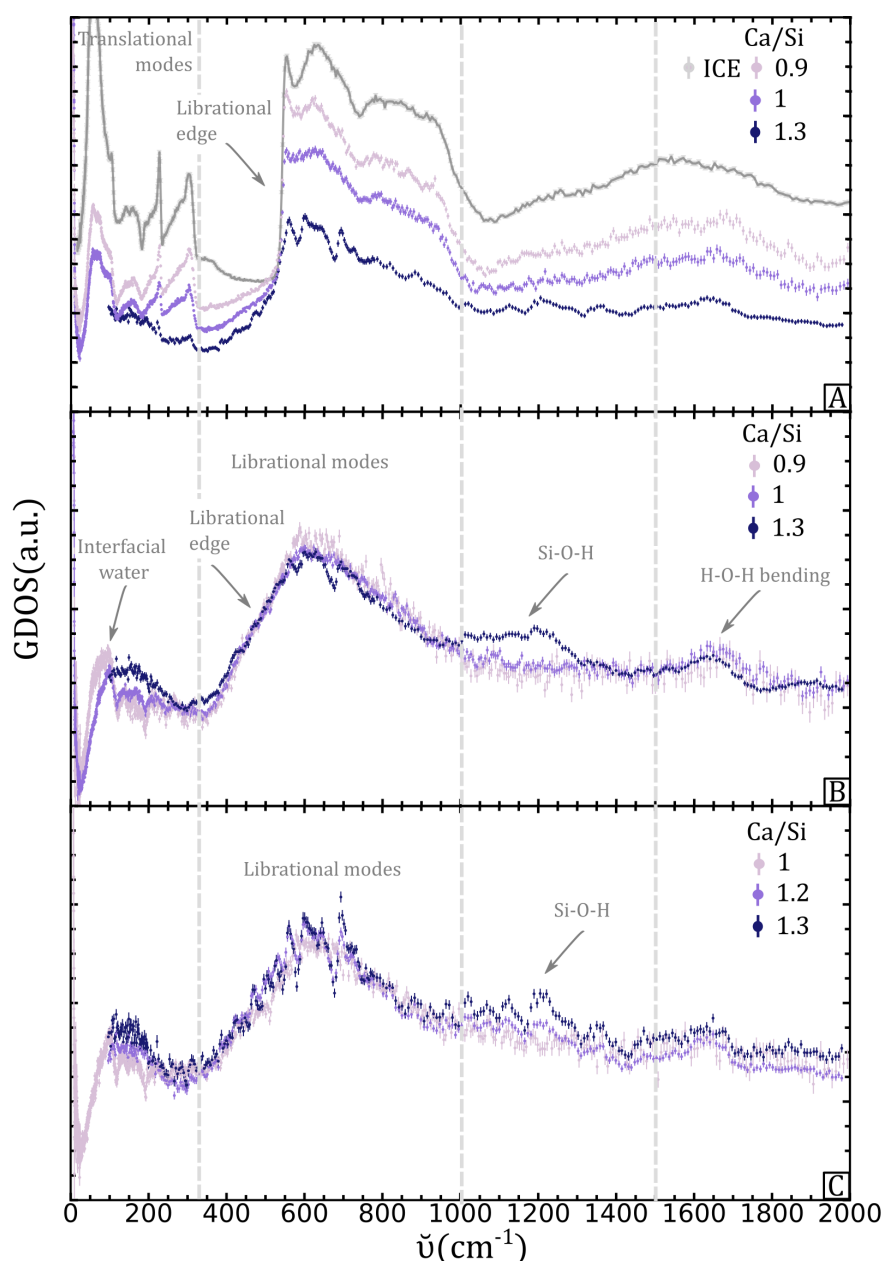


Figure 5. Experimental generalized density of states for C-(A)-S-H samples with varying RH levels and Ca/Si ratios. (A) 98RH samples show less ice-like features and more structured water increasing Ca/Si ratios. Librational edges at higher Ca/Si ratios reflect a greater abundance of interfacial and interlayer water and a smaller abundance of bulk-liquid-like capillary water; (B) In 55RH samples, an interfacial water signal at 96 cm^{-1} (12 meV) is observed, which is proportional to the amount of adsorbed interfacial water. Samples with lower Ca/Si ratios tend to exhibit slightly higher intensities for this peak. (C) DD samples show an increasing Si-O-H signal with increasing Ca/Si ratio.

The 'wet' FH C-S-H samples show a steep decrease in the amount of adsorbed water at increasing Ca/Si ratios as witnessed from both TGA and WSI experiments. The 'dry' C-S-H samples show a smaller difference in the amount of adsorbed water at rising Ca/Si ratios as seen by the amount of water in 55% RH samples from TGA and WSI (Table 1). These trends correlate well with the IINS data, where in the case of 98RH samples we can follow the increasing amounts of adsorbed water with decreasing Ca/Si ratios (Figure 5A).

However, the conditioning protocol (Figure S1 in the Supporting Information) has an effect on the total amount of adsorbed water as a function of Ca/Si (Table 1). As noted earlier, the equilibration time is an important factor when the adsorption of water in C-(A)-S-H is discussed⁸⁸. As Badmann et al. (1981) noted in their work, at RH levels > 95% RH adsorption is superimposed by capillary condensation, therefore the adsorbed volume is more a function of time than humidity⁷⁶. The longer exposure to a higher RH atmosphere of CASH_0.9 could have affected the amount of water adsorbed compared to CSH_1 and CSH_1.3.

The same logic can be applied to the 55RH samples (Figure 5B), where the relative decrease in area is less apparent than for 98RH samples. The CASH_0.9_55RH sample contains about 1.9 times more adsorbed water than CSH_1 and CSH_1.3 samples. This property of C-(A)-S-H to adsorb less water at higher Ca/Si ratios can be explained by the decreasing surface area shown in Table 1. Gaboreau et al. (2020) showed with XRD analysis that the stacking of the C-S-H layers increased from 3-6 to about 8 as the ratio of Ca/Si increases from 1 to 1.2⁷. The authors also observed a decreasing SSA calculated from WSI data with rising Ca/Si ratio^{7,8}, albeit acknowledging that effects such as interstratification (stacking of structurally different layers along c^* axis) and turbostratic stacking (random rotations of layers) could affect the results⁹⁰.

Based on the above discussion, we argue that the amount of adsorbed water is a delicate balance between the equilibration time and available surface area. On the other hand, the distribution of the adsorbed water is most probably affected by an increased number of Ca^{2+} ions, not only in the interlayers but also on the surfaces of C-(A)-S-H. These calcium ions form hydrophilic sites for water that are highly structured.

Finally, the comparison of DD samples at different Ca/Si ratios (Figure 5C) shows that they have matching intensities, except for the region around 1100 cm^{-1} (136.4 meV). This intensity is characteristic of silanol hydroxyl groups as shown for different minerals⁵³.

In summary, we have applied the IINS experiment to probe the dynamics of water in our C-(A)-S-H samples with three Ca/Si ratios (0.9, 1, 1.3) at five hydration levels. The resulting GDOS allows us to distinguish different types of water present in our samples: interfacial and interlayer water strongly affected by C-(A)-S-H surfaces; bulk-liquid-like capillary pore water, resembling ice Ih; and intermediate samples containing both multilayer interfacial and bulk-like water. The method permits the observation of characteristic bands coming from translational movements, bending and stretching motions of water molecules, and most importantly, from librational motions (H-bond hindered translations and rotations of water molecules).

4.3. Computed IINS data

To complement our experimental IINS data, we performed classical MD simulations and calculated the associated generalized density of states (GDOS). Predicted GDOS were calculated for different hydrogen populations reflecting different water distributions in our ‘wet’ and ‘dry’ C-(A)-S-H samples. We used two atomistic C-S-H models developed in our previous work³⁷: a ‘dry’ atomic model named ‘CSH-dry-NP’ with H₂O/Si ratio of 1.35 and interlayer spacing $d_{001\text{-MD}} = 11.0(2)$ Å and a fully hydrated model ‘CSH-wet-NP’ with H₂O/Si ratio of 38.5 and an interlayer spacing $d_{001\text{-MD}} = 13.0(2)$ Å. The direct comparison of the GDOS calculated from our MD simulation trajectories with our measured vibrational spectra is consistent with our experimental conclusions. Moreover, water diffusion coefficients calculated for our ‘CSH-dry-NP’ model confirms the presence of the highly bound interfacial/interlayer water in our ‘dry’ C-(A)-S-H samples.

Bulk water vs interfacial and interlayer water

GDOS were calculated for all populations of hydrogen atoms (water and hydroxyl hydrogens) in the ‘CSH-dry-NP’ model and the bulk water (Figure S4 in the Supporting Information). The shapes and intensities of the vibrational modes of water of the ‘CSH-dry-NP’ model are very different from the ones of bulk water. Differences are present in all regions of the spectra: at lower frequencies we observe a peak at 260 cm^{-1} ($\sim 32.2\text{ meV}$), which is not present in bulk water, followed by librational modes having half the intensity of bulk water, and an additional broad peak centered around 1100 cm^{-1} (136.4 meV). The origins of these signals will be addressed later. Intramolecular vibrations are observed at higher frequencies, including the H-O-H bending peak generally expected at around 1600 cm^{-1} (198.4 meV) and the O-H stretching signal at around 3600 cm^{-1} (446.3 meV).

The bending peak for the calculated bulk water is centered at the expected value 1650 cm^{-1} , whilst the bending in CSH_1_55RH is split into two, occurring at about 1725 and 1830 cm^{-1} (213.5 meV and 226.5 meV), indicating a clear deviation from the bulk water. The stretching modes for bulk water are centered at 3730 cm^{-1} (462.4 meV) and 3810 cm^{-1} (472.4 meV), and for the ‘CSH-dry-NP’ model at 3677 and 3830 cm^{-1} (455.9 and 474.8 meV). A blue shift for the expected stretching values is most probably due to the limitations of the SPC water model, in addition to the interlayer and interfacial water properties in ‘CSH-dry-NP’.

The calculated total GDOS of the ‘CSH-dry-NP’ system consists of contributions from hydrogens of water and hydrogens of structural hydroxyls. Since there are 132 hydroxyl hydrogens and 896 water hydrogens in the simulated ‘dry’ system, the total GDOS signal is dominated by the hydrogens of molecular water (Figure S5 in the Supporting Information).

Experimental IINS data vs MD calculated GDOS data

Here, we compare the experimental data to our calculated GDOS and evaluate whether the comparison is consistent with the conclusions made in the experimental section.

The GDOS of water hydrogens can be separated depending on the local environment of the H atoms: (A) water hydrogens in the first hydration shell of calcium ions, and/or forming H-bonds with the C-S-H surfaces; (B) hydrogens forming hydrogen bonds with other water molecules and; (C) hydrogens not involved in any kind of bonding (Figure S6 in the Supporting Information). These different types of hydrogens result in IINS signals at different energies as shown in Figure 6.

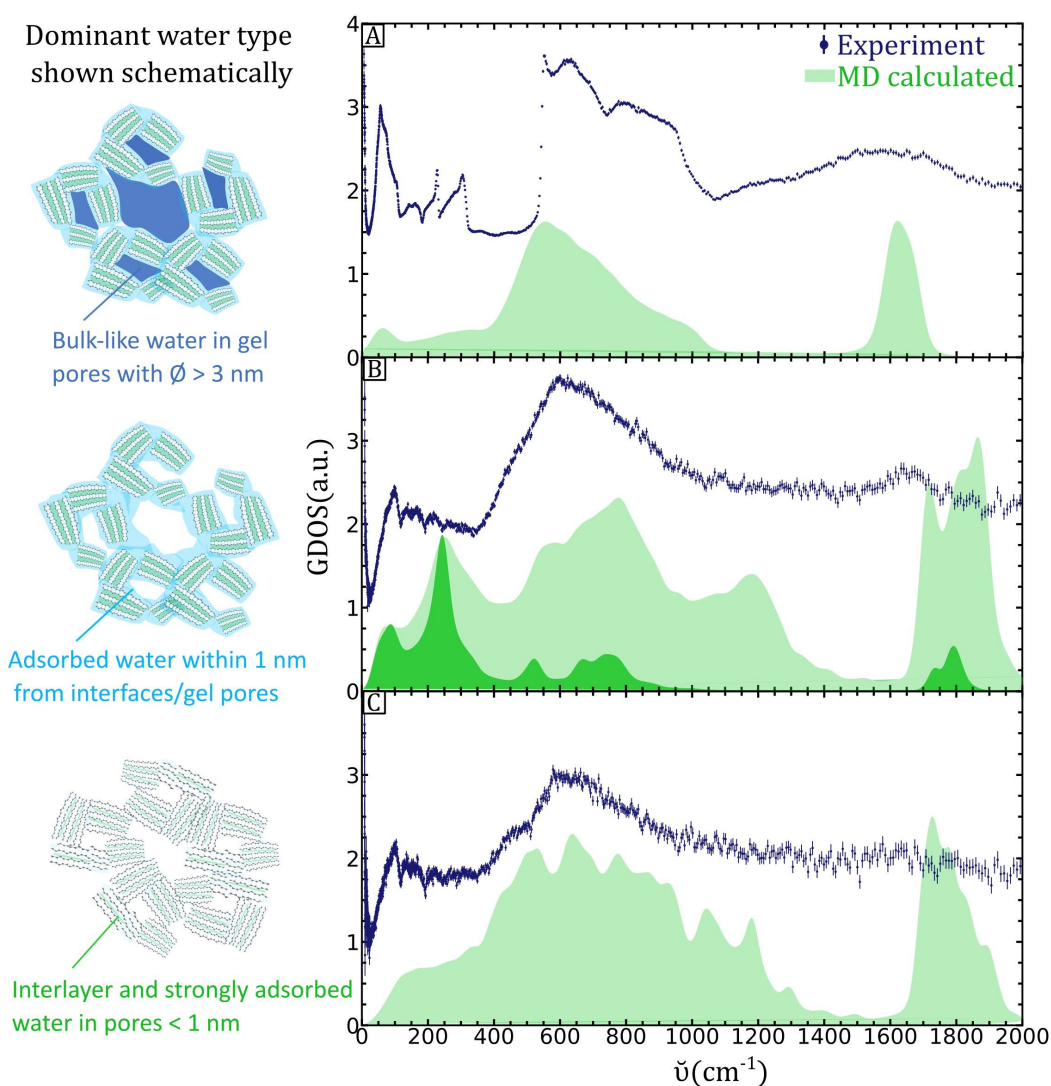


Figure 6. (right) Experimental and calculated GDOS for CSH_1 samples with varying water content (A) FH; (B) 55RH; (C) DD; (left) Schematic images of C-(A)-S-H containing different water types: strongly bound interlayer and interfacial water are in green; adsorbed multilayer interfacial water is in light blue; bulk-like capillary pore water are in dark blue. (A) The experimental FH spectrum is dominated by the bulk-like capillary water found in gel pores larger than ~ 3 nm. The MD simulated GDOS reproduces a characteristic peak at 80 cm^{-1} (10 meV) attributed to the translations of water molecules in ice Ih, a sharp librational edge starting at $\sim 550 \text{ cm}^{-1}$ (68 meV), and the H-O-H bending modes at 1650 cm^{-1} (206 meV); (B) The experimental 55RH spectrum

is dominated by adsorbed interfacial water found on the surfaces of gel pores within about 1 nm from the C-(A)-S-H interfaces. The MD simulated GDOS of total water in CSH_1_55RH nanoparticle model containing interfacial and interlayer water is shown in light green. The MD-generated partial GDOS (shaded dark green) represents interfacial dangling water hydrogen atoms with characteristic signals at 96 cm^{-1} and 245 cm^{-1} (12 and 30 meV). H-O-H bending modes in the 55RH sample are at 1650 cm^{-1} in the experimental spectrum, and at 1800 cm^{-1} in MD generated one; (C) The experimental DD spectra is dominated by strongly bound interlayer water in pores smaller than 1 nm, and interfacial water within 1 nm (e.g., 3 water monolayers) from the C-(A)-S-H surfaces. The MD-generated partial GDOS represents interlayers of the CSH_1_55RH nanoparticle model. The absence of the peaks at 96 cm^{-1} and 245 cm^{-1} confirms that they are associated interfacial water.

The lower frequency ($<300 \text{ cm}^{-1}$) contributions originate mainly from the dangling water hydrogens and from the water molecules H-bonded to other water molecules, as demonstrated in light blue in Figure 6. The signal at about 55 cm^{-1} (7 meV) in ice decreases in intensity and broadens for samples containing interfacial and interlayer water. Our calculated GDOS shows these peaks at 80 cm^{-1} (9.9 meV) and 260 cm^{-1} (32.2 meV) come from the dangling interfacial water hydrogens and H-bonded interfacial water molecules. Moreover, when only the interlayer region is selected in the 'CSH-dry-NP' and 'CSH-wet-NP' models, these lower energy signals disappear (Figure S7 in the Supporting Information), meaning that there are no dangling water hydrogens in the interlayer region. These dangling interfacial hydrogens are responsible for an extra peak at $\sim 249 \text{ cm}^{-1}$ present only in oven-dried samples (bright green on Figures 2A/B). Most probably this peak signifies a monolayer of adsorbed interfacial water (hence dangling hydrogens), which stems from the wetting mechanism of the C-(A)-S-H surfaces as evidenced by our MD simulations.

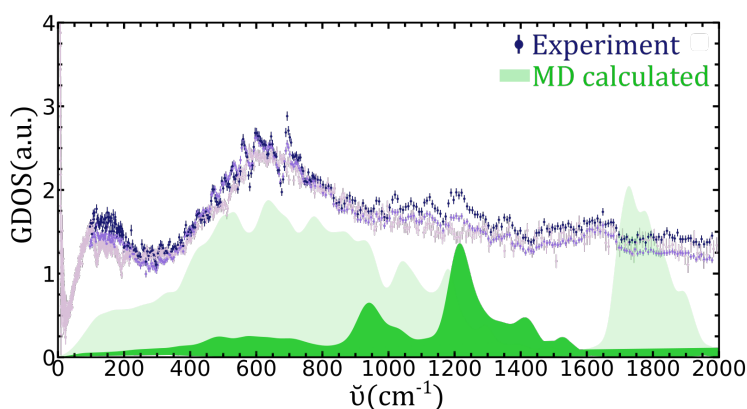


Figure 7. (Blue and purple symbols) Experimental IINS spectra for DD CSH_1, CSH_1.2, and CSH_1.3; (Shaded light green area) Calculated GDOS of interlayer hydrogens show the absence of interfacial hydrogen peaks at 80 cm^{-1} (9.9 meV) and 260 cm^{-1} (32.2 meV); (Shaded dark green area) Calculated partial GDOS of interlayer hydroxyl hydrogen atoms showing intensity to the signal centered at 1100 cm^{-1} .

We calculated the vibrational density of states for the silanol hydroxyls⁵³ found in the interlayer that showed the intensity centered at 1100 cm^{-1} (136.4 meV) (Figure 7). This signal increases with the Ca/Si ratios. Recent findings based on ^1H NMR experiments and theoretical calculations

showed similar trends⁹¹. It is known that at higher Ca/Si ratios the number of defects increases as evidenced by the increased number of Q¹ silicons (Si atoms connected only to another Si atom) and mean length of Si chain (the mean number of silica tetrahedra forming chains)⁹². We found that the 1100 cm⁻¹ (from 900 to 1400cm⁻¹) signal in DD samples increases consistently from CSH_1 to CSH_1.2 to CSH_1.3.

These hydroxyl signals do not arise from calcium hydroxide-like species. We have verified the absence of portlandite by comparing the IINS spectra of portlandite (Ca(OH)₂) with our C-(A)-S-H spectra. Portlandite generally shows an intense peak at 330 cm⁻¹ (41 meV) and is clearly visible in INS spectra of cement pastes with higher Ca/Si ratios (Ca/Si > 1.6¹⁸). Although it remains difficult to assign these signals definitively to the silanol hydroxyls as previous literature points to the opposite trends of the number of Si-OH decreasing with increasing Ca/Si ratios^{5,93}. Careful analysis of our results suggests that silanol hydroxyl groups in C-(A)-S-H show increased signal intensity at higher Ca/Si due to an increased number of defects at higher Ca/Si ratios.

Diffusion of water in 'CSH-dry-NP'

The trajectories of oxygen atoms of water were followed over 5 ns, revealing a very restricted motion over the course of the production run (Figure 8A). The mean square displacement (MSD) of water molecules in the 'CSH-dry-NP' system (Figure 8B) has been used to calculate the self-diffusion coefficient of interfacial water. The obtained value of 6.8×10^{-11} m²/s compares well to other reported values (from 2.6 to 5×10^{-11} m²/s) for interfacial/confined water in C-S-H³⁰.

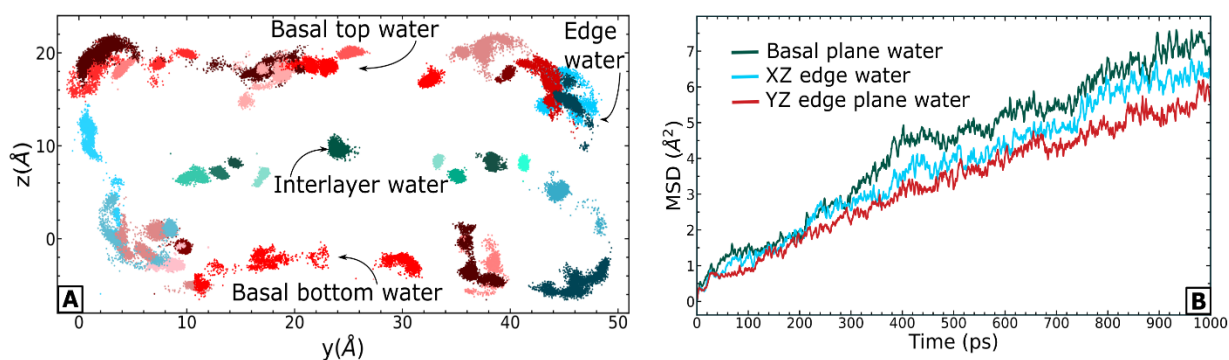


Figure 8. (A) The trajectories of water oxygens followed for 5 ns shown in the YZ plane for 'CSH-dry-NP'; (B) The MSD of water molecules on the 'CSH-dry-NP' interfaces during 1 ns.

5 CONCLUSIONS

Inelastic Incoherent Neutrons Scattering experiment, complemented with MD simulations, WSI, and TGA data, is a powerful approach to probe the vibrational dynamics of water in confined systems such as C-(A)-S-H surfaces and pores. The spectra exhibit a range of features that allow attributing different properties to the water in the different regions of the samples. Our combined

approach shows that at lower energies ($<300\text{ cm}^{-1}$ or 37.2 meV) the so-called ‘fingerprint’ signal of confined water at around 80 cm^{-1} (9.9 meV) was present in the ‘dry’ C-(A)-S-H samples, with the oven-dried samples showing a peak at 260 cm^{-1} (32.2 meV) possibly belonging to a thin monolayer of interfacial water. At intermediate energies, the shape of the librational region is different for water confined at interfaces, showing a broadband that starts at $\sim 300\text{ cm}^{-1}$ (37.2 meV), as opposed to 550 cm^{-1} (68.2 meV) for bulk-like water. A linear combination fitting was applied to fit 98RH samples as a mixture of multilayer adsorbed and bulk-liquid-like water. The high energy ($>1000\text{ cm}^{-1}$ or 124 meV) intermolecular bending and stretching modes are present in the experimental data but with significantly dampened intensities. The calculated GDOS reproduced these intermolecular vibrations, albeit blue-shifted due to the nature of confined water in our dry samples, and approximations associated with the SPC water model.

Differences in both the amount and the distribution of adsorbed water were found when increasing the Ca/Si ratio. At 98% RH, CSH_1.3 samples adsorbed significantly less water than CSH_1, which in turn adsorbed less water than CASH_0.9. The water at higher Ca/Si ratios was also more structured, i.e., less bulk-liquid-like. This observation can be rationalized by considering the number of adsorption sites for water present in the different samples. At high Ca/Si ratios, more Ca^{2+} is present in the samples. This cation acts as a strong center of charge, very hydrophilic in nature, thus creating more adsorption sites for water. This water is not only bonded to the Ca^{2+} cation, but it also forms hydrogen bonds with oxygen atoms from the structure.

Confined, strongly bound, water from the first coordination sphere of Ca^{2+} has limited diffusivity and forms strong hydrogen bonds with surface oxygen atoms, in particular in the interlayer region. Previous studies have reported an increase of the stacking along the c^* direction upon the increase of the Ca/Si ratio in the samples. This increased stacking could lead to an eventual higher crystallinity, with better-defined sites for water adsorption (water from the Ca^{2+} hydration shell).

Overall, our experimental and simulation results converge towards a picture where the evolution from thin layers of adsorbed water to bulk capillary water is dampened by the structure of C-(A)-S-H, in particular by the availability of Ca^{2+} sites that tend to keep the water in the form of structured surface layers.

Determining the range of humidity at which bulk-like water is present in C-(A)-S-H samples is of major importance to understand better some of the mechanisms that take present or controlled by the properties of C-(A)-S-H – water interfaces. This is the case, for instance, of the carbonation reaction that takes place in the presence of dissolved CO_2 . As in a saturated system, the presence of capillary water tends to lead to dissolution–reprecipitation processes, unlike the solid-state

transformation that takes place under non-saturated conditions⁹⁴. It is expected that other processes, such as creep, can be influenced by the presence of adsorbed vs. bulk-like water⁹⁵.

6 ACKNOWLEDGEMENTS

Use of the Geochemistry-Mineralogy platform at ISTerre is acknowledged. A.F.-M. and A.E.S.V.-D. acknowledge funding from the ANR-JCJC 'NUANCE' project (grant ANR-17-CE08-0057). We thank the IDEX mobility scholarship program of the University of Grenoble-Alpes for supporting a research stay at Princeton University. We thank the Institut Laue-Langevin, ISIS Neutron and Muon Source, and European Synchrotron Radiation Facility for allocated beamtimes. I.C.B. was supported by the U.S. Department of Energy, Office of Science, Office of Basic Energy Sciences, Geosciences Program under Award DE-SC0018419. Molecular dynamics simulations were performed using resources of the National Energy Research Scientific Computing Center (NERSC), which is supported by the U.S. Department of Energy, Office of Science, under Award DE-AC02-05CH11231. Z.Z. thanks BRGM for cofounding her PhD and Dr. Arianna d'Angelo for fruitful discussions about DOS calculations.

REFERENCES:

- (1) Goracci, G.; Monasterio, M.; Jansson, H.; Cervený, S. Dynamics of Nano-Confined Water in Portland Cement - Comparison with Synthetic C-S-H Gel and Other Silicate Materials. *Sci. Rep.* **2017**, 7 (1), 8258. <https://doi.org/10.1038/s41598-017-08645-z>.
- (2) Vandamme, M.; Ulm, F.-J. Nanogranular Origin of Concrete Creep. *Proc. Natl. Acad. Sci.* **2009**, 106, 10552–10557.
- (3) Bordallo, H. N.; Aldridge, L. P.; Desmedt, A. Water Dynamics in Hardened Ordinary Portland Cement Paste or Concrete: From Quasielastic Neutron Scattering. *J. Phys. Chem. B* **2006**, 110 (36), 17966–17976. <https://doi.org/10.1021/jp062922f>.
- (4) Pinson, M. B.; Masoero, E.; Bonnaud, P. A.; Thomas, J. J.; Bazant, M. Z. Hysteresis from Multiscale Porosity: Modeling Water Sorption and Shrinkage in Cement Paste. *Phys. Rev. Appl.* **2015**, 3, 064009–066016.
- (5) Richardson, I. G. Tobermorite/Jennite- and Tobermorite/Calcium Hydroxide-Based Models for the Structure of C-S-H: Applicability to Hardened Pastes of Tricalcium Silicate, β -Dicalcium Silicate, Portland Cement, and Blends of Portland Cement with Blast-Furnace Slag, Metakaol. *Cem. Concr. Res.* **2004**, 34, 1733–1777.
- (6) Valori, A.; McDonald, P. J.; Scrivener, K. L. The Morphology of C-S-H: Lessons from ¹H Nuclear Magnetic Resonance Relaxometry. *Cem. Concr. Res.* **2013**, 49, 65–81.
- (7) Gaboreau, S.; Grangeon, S.; Claret, F.; Ihiawakrim, D.; Ersen, O.; Montouillout, V.; Maubec,

- 759 N.; Roosz, C.; Henocq, P.; Carteret, C. Hydration Properties and Interlayer Organization in
760 Synthetic C-S-H. *Langmuir* **2020**, *36*, 9449–9464.
- 761 (8) Roosz, C.; Gaboreau, S.; Grangeon, S.; Prêt, D.; Montouillout, V.; Maubec, N.; Ory, S.; Blanc,
762 P.; Vieillard, P.; Henocq, P. Distribution of Water in Synthetic Calcium Silicate Hydrates.
763 *Langmuir* **2016**, *32*, 6794–6805.
- 764 (9) McDonald, P. J.; Rodin, V.; Valori, A. Characterisation of Intra- and Inter-C-S-H Gel Pore
765 Water in White Cement Based on an Analysis of NMR Signal Amplitudes as a Function of
766 Water Content. *Cem. Concr. Res.* **2010**, *40*, 1656–1663.
- 767 (10) McDonald, P. J.; Korb, J.-P.; Mitchell, J.; Monteilhet, L. Surface Relaxation and Chemical
768 Exchange in Hydrating Cement Pastes: A Two-Dimensional NMR Relaxation Study. *Phys.*
769 *Rev. E* **2005**, *72* (1), 11409. <https://doi.org/10.1103/PhysRevE.72.011409>.
- 770 (11) Hu, Z.; Wyrzykowski, M.; Scrivener, K.; Lura, P. A Novel Method to Predict Internal Relative
771 Humidity in Cementitious Materials by ¹H NMR. *Cem. Concr. Res.* **2017**, No. November, 1–
772 14. <https://doi.org/10.1016/j.cemconres.2017.11.001>.
- 773 (12) Barberon, F.; Korb, J. P.; Petit, D.; Morin, V.; Bermejo, E. Probing the Surface Area of a
774 Cement-Based Material by Nuclear Magnetic Relaxation Dispersion. *Phys. Rev. Lett.* **2003**,
775 *90* (11), 4. <https://doi.org/10.1103/PhysRevLett.90.116103>.
- 776 (13) Monteilhet, L.; Korb, J.-P.; Mitchell, J.; McDonald, P. J. Observation of Exchange of Micropore
777 Water in Cement Pastes by Two-Dimensional T(2)-T(2) Nuclear Magnetic Resonance
778 Relaxometry. *Phys. Rev. E. Stat. Nonlin. Soft Matter Phys.* **2006**, *74* (6 Pt 1), 61404.
779 <https://doi.org/10.1103/PhysRevE.74.061404>.
- 780 (14) Blinc, R.; Burgar, M.; Lahajnar, G.; Rozmarin, M.; Rutar, V.; Kocuvan, I.; Ursic, J. NMR
781 Relaxation Study of Adsorbed Water in Cement and C3S Pastes. *J. Am. Ceram. Soc.* **1978**, *61*
782 (1–2), 35–37. <https://doi.org/https://doi.org/10.1111/j.1151-2916.1978.tb09224.x>.
- 783 (15) Ridi, F.; Fratini, E.; Milani, S.; Baglioni, P. Near-Infrared Spectroscopy Investigation of the
784 Water Confined in Tricalcium Silicate Pastes. *J. Phys. Chem. B* **2006**, *110* (33), 16326–
785 16331. <https://doi.org/10.1021/jp060026y>.
- 786 (16) Cervený, S.; Arrese-Igor, S.; Dolado, J. S.; Gaitero, J. J.; Alegria, A.; Colmenero, J. Effect of
787 Hydration on the Dielectric Properties of C-S-H Gel. *J. Chem. Phys.* **2011**, *134* (3).
788 <https://doi.org/10.1063/1.3521481>.
- 789 (17) FitzGerald, S. A.; Neumann, D. A.; Rush, J. J.; Kirkpatrick, R. J.; Cong, X.; Livingston, R. A.
790 Inelastic Neutron Scattering Study of the Hydration of Tricalcium Silicate. *J. Mater. Res.*

- 791 **1999**, *14* (3), 1160–1165. <https://doi.org/D0I: 10.1557/JMR.1999.0154>.
- 792 (18) Thomas, J. J.; Chen, J. J.; Jennings, H. M.; Neumann, D. A. Ca-OH Bonding in the C-S-H Gel
793 Phase of Tricalcium Silicate and White Portland Cement Pastes Measured by Inelastic
794 Neutron Scattering. *Chem. Mater.* **2003**, *15* (20), 3813–3817.
795 <https://doi.org/10.1021/cm034227f>.
- 796 (19) Nemes, N. M.; Neumann, D. A.; Livingston, R. A. States of Water in Hydrated C3S (Tricalcium
797 Silicate) as a Function of Relative Humidity. *J. Mater. Res.* **2006**, *21*, 2516–2523.
- 798 (20) Livingston, R.; Neumann, D.; Allen, A.; RUSH, J. Application of Neutron Scattering Methods
799 to Cementitious Materials. *MRS Proc.* **1994**, *376*, 459. [https://doi.org/doi:10.1557/PROC-](https://doi.org/doi:10.1557/PROC-376-459)
800 [376-459](https://doi.org/doi:10.1557/PROC-376-459).
- 801 (21) Amann-Winkel, K.; Bellissent-Funel, M.-C.; Bove, L. E.; Loerting, T.; Nilsson, A.; Paciaroni,
802 A.; Schlesinger, D.; Skinner, L. X-Ray and Neutron Scattering of Water. *Chem. Rev.* **2016**,
803 *116* (13), 7570–7589. <https://doi.org/10.1021/acs.chemrev.5b00663>.
- 804 (22) Bellissent-Funel, M.-C.; Chen, S. H.; Zanotti, J.-M. Single-Particle Dynamics of Water
805 Molecules in Confined Space. *Phys. Rev. E* **1995**, *51* (5), 4558–4569.
806 <https://doi.org/10.1103/PhysRevE.51.4558>.
- 807 (23) Berg, M. C.; Dalby, K. N.; Tsapatsaris, N.; Okhrimenko, D. V.; Sørensen, H. O.; Jha, D.; Embs,
808 J. P.; Stipp, S. L. S.; Bordallo, H. N. Water Mobility in Chalk: A Quasielastic Neutron Scattering
809 Study. *J. Phys. Chem. C* **2017**, *121* (26), 14088–14095.
810 <https://doi.org/10.1021/acs.jpcc.7b01998>.
- 811 (24) Crupi, V.; Majolino, D.; Migliardo, P.; Venuti, V.; Bellissent-Funel, M. C. Structure and
812 Dynamics of Water Confined in a Nanoporous Sol-Gel Silica Glass: A Neutron Scattering
813 Study. *Mol. Phys.* **2003**, *101* (22), 3323–3333.
814 <https://doi.org/10.1080/00268970310001638790>.
- 815 (25) Hunvik, K. W. B.; Loch, P.; Cavalcanti, L. P.; Seljelid, K. K.; Røren, P. M.; Rudić, S.; Wallacher,
816 D.; Kirch, A.; Knudsen, K. D.; Rodrigues Miranda, C.; Breu, J.; Bordallo, H. N.; Fossum, J. O.
817 CO₂ Capture by Nickel Hydroxide Interstratified in the Nanolayered Space of a Synthetic
818 Clay Mineral. *J. Phys. Chem. C* **2020**, *124* (48), 26222–26231.
819 <https://doi.org/10.1021/acs.jpcc.0c07206>.
- 820 (26) Faraone, A.; Fratini, E.; Baglioni, P.; Chen, S. H. Quasielastic and Inelastic Neutron Scattering
821 on Hydrated Calcium Silicate Pastes. *J. Chem. Phys.* **2004**, *121* (7), 3212–3220.
822 <https://doi.org/10.1063/1.1772755>.

- 823 (27) Bellissent-Funel, M. C.; Chen, S. H.; Zanotti, J. M. Single-Particle Space. *Phys. Rev. E* **1995**, 51
824 (5), 4558–4569.
- 825 (28) Abdolhosseini Qomi, M.; Krakowiak, K. J.; Bauchy, M.; Stewart, K. L.; Shahsavari, R.;
826 Jagannathan, D.; Brommer, D. B.; Baronnet, A.; Buehler, M. J.; Yip, S.; Ulm, F.-J.; Van Vliet, K.
827 J.; Pellenq, R. -. M. Combinatorial Molecular Optimization of Cement Hydrates. *Nat.*
828 *Commun.* **2014**, 5, 4960.
- 829 (29) Youssef, M.; Pellenq, R. J. M.; Yildiz, B. Glassy Nature of Water in an Ultraconfining
830 Disordered Material: The Case of Calcium-Silicate-Hydrate. *J. Am. Chem. Soc.* **2011**, 133,
831 2499–2510.
- 832 (30) Abdolhosseini Qomi, M. J.; Brochard, L.; Honorio, T.; Maruyama, I.; Vandamme, M. Advances
833 in Atomistic Modeling and Understanding of Drying Shrinkage in Cementitious Materials.
834 *Cem. Concr. Res.* **2021**, 148 (January), 106536.
835 <https://doi.org/10.1016/j.cemconres.2021.106536>.
- 836 (31) Kalinichev, A. G.; Wang, J.; Kirkpatrick, R. J. Molecular Dynamics Modeling of the Structure,
837 Dynamics and Energetics of Mineral-Water Interfaces: Application to Cement Materials.
838 *Cem. Concr. Res.* **2007**, 37, 337–347.
- 839 (32) Taylor, H. F. W. Proposed Structure for Calcium Silicate Hydrate Gel. *J. Am. Ceram. Soc.*
840 **1986**, 69 (6), 464–467. <https://doi.org/10.1111/j.1151-2916.1986.tb07446.x>.
- 841 (33) Korb, J.-P.; Whaley Hodges, M.; Bryant, R. Translational Diffusion of Liquids at Surface of
842 Microporous Materials: New Theoretical Analysis of Field Cycling Magnetic Relaxation
843 Measurements. *Magn. Reson. Imaging* **1998**, 16 (5), 575–578.
844 [https://doi.org/https://doi.org/10.1016/S0730-725X\(98\)00051-4](https://doi.org/https://doi.org/10.1016/S0730-725X(98)00051-4).
- 845 (34) Kupwade-Patil, K.; Bumajdad, A.; Brown, C. M.; Tyagi, M.; Butch, N. P.; Jamsheer, A. F.;
846 Büyüköztürk, O. New Insights into Water Dynamics of Portland Cement Paste with Nano-
847 Additives Using Quasielastic Neutron Scattering. *J. Mater. Sci.* **2019**, 54 (6), 4710–4718.
848 <https://doi.org/10.1007/s10853-018-03212-x>.
- 849 (35) Le, P.; Fratini, E.; Ito, K.; Wang, Z.; Mamontov, E.; Baglioni, P.; Chen, S.-H. Dynamical
850 Behaviors of Structural, Constrained and Free Water in Calcium- and Magnesium-Silicate-
851 Hydrate Gels. *J. Colloid Interface Sci.* **2016**, 469, 157–163.
852 <https://doi.org/https://doi.org/10.1016/j.jcis.2016.01.071>.
- 853 (36) Bordallo, H. N.; Aldridge, L. P.; Churchman, G. J.; Gates, W. P.; Telling, M. T. F.; Kiefer, K.;
854 Fouquet, P.; Seydel, T.; Kimber, S. A. J. Quasi-Elastic Neutron Scattering Studies on Clay

- 855 Interlayer-Space Highlighting the Effect of the Cation in Confined Water Dynamics. *J. Phys.*
856 *Chem. C* **2008**, *112* (36), 13982–13991. <https://doi.org/10.1021/jp803274j>.
- 857 (37) Zhakiyeva, Z.; Cuello, G. J.; Fischer, H. E.; Bowron, D. T.; Dejoie, C.; Magnin, V.; Campillo, S.;
858 Bureau, S.; Poulain, A.; Besselink, R.; Gaboreau, S.; Grangeon, S.; Claret, F.; Bourg, I. C.; Van
859 Driessche, A. E. S.; Fernandez-Martinez, A. Structure of Water Adsorbed on Nanocrystalline
860 Calcium Silicate Hydrate Determined from Neutron Scattering and Molecular Dynamics
861 Simulations. *J. Phys. Chem. C* **2022**, *under revi.*
- 862 (38) Haas, J.; Nonat, A. From C-S-H to C-A-S-H: Experimental Study and Thermodynamic
863 Modelling. *Cem. Concr. Res.* **2015**, *68*, 124–138.
- 864 (39) Roos, C.; Vieillard, P.; Blanc, P.; Gaboreau, S.; Gailhanou, H.; Braithwaite, D.; Montouillout,
865 V.; Denoyel, R.; Henocq, P.; Madé, B. Thermodynamic Properties of C-S-H, C-A-S-H and M-
866 S-H Phases: Results from Direct Measurements and Predictive Modelling. *Appl.*
867 *Geochemistry* **2018**, *92*, 140–156.
- 868 (40) Feldman, R. F.; Sereda, P. J. A New Model for Hydrated Portland Cement and Its Practical
869 Implications. *Eng. J.* **1970**, *53*, 53–59.
- 870 (41) Brunauer, S.; Emmett, P. H.; Teller, E. Adsorption of Gases in Multimolecular Layers. *J. Am.*
871 *Chem. Soc.* **1938**, *60*, 309–319.
- 872 (42) Kieffer, J.; Wright, J. P. PyFAI: A Python Library for High Performance Azimuthal
873 Integration on GPU. *Powder Diff.* **2013**, *28*, S339–S350.
- 874 (43) Toby, B. H.; Dreele, R. B. Von. GSAS-II: The Genesis of a Modern Open-Source All Purpose
875 Crystallography Software Package. **2013**, 544–549.
- 876 (44) Jiménez-Ruiz, M.; Ivanov, A.; Fuard, S. LAGRANGE - The New Neutron Vibrational
877 Spectrometer at the ILL. *J. Phys. Conf. Ser.* **2014**, *549* (1). [https://doi.org/10.1088/1742-
878 *6596/549/1/012004*.](https://doi.org/10.1088/1742-6596/549/1/012004)
- 879 (45) Ivanov, A.; Jimenez-Ruiz, M.; Kulda, J. IN1-Lagrange-the New ILL Instrument to Explore
880 Vibration Dynamics of Complex Materials. *J. Phys. Conf. Ser.* **2014**, *554* (1), 1–7.
881 <https://doi.org/10.1088/1742-6596/554/1/012001>.
- 882 (46) Richard, D.; Ferrand, M.; Kearley, G. J. Analysis and Visualisation of Neutron-Scattering
883 Data. *J. Neutron Res.* **1996**, *4*, 33–39. <https://doi.org/10.1080/10238169608200065>.
- 884 (47) Parker, S. F.; Fernandez-Alonso, F.; Ramirez-Cuesta, A. J.; Tomkinson, J.; Rudic, S.; Pinna, R.
885 S.; Gorini, G.; Fernández Castañon, J. Recent and Future Developments on TOSCA at ISIS. *J.*

- 886 *Phys. Conf. Ser.* **2014**, 554 (1). <https://doi.org/10.1088/1742-6596/554/1/012003>.
- 887 (48) Pinna, R. S.; Rudić, S.; Parker, S. F.; Armstrong, J.; Zanetti, M.; Škoro, G.; Waller, S. P.; Zacek,
888 D.; Smith, C. A.; Capstick, M. J.; McPhail, D. J.; Pooley, D. E.; Howells, G. D.; Gorini, G.;
889 Fernandez-Alonso, F. The Neutron Guide Upgrade of the TOSCA Spectrometer. *Nucl.*
890 *Instruments Methods Phys. Res. Sect. A Accel. Spectrometers, Detect. Assoc. Equip.* **2018**, 896
891 (March), 68–74. <https://doi.org/10.1016/j.nima.2018.04.009>.
- 892 (49) STFC. Mantid <https://www.mantidproject.org/>.
- 893 (50) Plimpton, S. Fast Parallel Algorithms for Short-Range Molecular Dynamics. *J. Comput. Phys.*
894 **1997**, 117, 1–42.
- 895 (51) Berendsen, H. J. C.; Grigera, J. R.; Straatsma, T. P. The Missing Term in Effective Pair
896 Potentials. *J. Phys. Chem.* **1987**, 91, 6269–6271.
- 897 (52) Cygan, R. T.; Liang, J. J.; Kalinichev, A. G. Molecular Models of Hydroxide, Oxyhydroxide, and
898 Clay Phases and the Development of a General Force Field. *J. Phys. Chem. B* **2004**, 108,
899 1255–1266.
- 900 (53) Cygan, R. T.; Greathouse, J. A.; Kalinichev, A. G. Advances in Clayff Molecular Simulation of
901 Layered and Nanoporous Materials and Their Aqueous Interfaces. *J. Phys. Chem. C* **2021**,
902 125 (32), 17573–17589. <https://doi.org/10.1021/acs.jpcc.1c04600>.
- 903 (54) Wang, J.; Kalinichev, A. G.; Kirkpatrick, R. J.; Cygan, R. T. Structure, Energetics, and
904 Dynamics of Water Adsorbed on the Muscovite (001) Surface: A Molecular Dynamics
905 Simulation. *J. Phys. Chem. B* **2005**, 109, 15893–15905.
- 906 (55) Bourg, I. C.; Sposito, G. Molecular Dynamics Simulations of the Electrical Double Layer on
907 Smectite Surfaces Contacting Concentrated Mixed Electrolyte (NaCl-CaCl(2)) Solutions. *J.*
908 *Colloid Interface Sci.* **2011**, 360, 701–715.
- 909 (56) Bourg, I. C.; Steefel, C. I. Molecular Dynamics Simulations of Water Structure and Diffusion
910 in Silica Nanopores. *J. Phys. Chem. C* **2012**, 116, 11556–11564.
- 911 (57) Ferrage, E.; Lanson, B.; Michot, L. J.; Robert, J. L. Hydration Properties and Interlayer
912 Organization of Water and Ions in Synthetic Na-Smectite with Tetrahedral Layer Charge.
913 Part 1. Results from X-Ray Diffraction Profile Modeling. *J. Phys. Chem. C* **2010**, 114, 4515–
914 4526.
- 915 (58) Ockwig, N. W.; Cygan, R. T.; Criscenti, L. J.; Nenoff, T. M. Molecular Dynamics Studies of
916 Nanoconfined Water in Clinoptilolite and Heulandite Zeolites. *Phys. Chem. Chem. Phys.*

- 917 **2008**, *10*, 800–807.
- 918 (59) Roscioni, O. M.; Muccioli, L.; Zannoni, C. Predicting the Conditions for Homeotropic
919 Anchoring of Liquid Crystals at a Soft Surface. 4-n-Pentyl-4'-Cyanobiphenyl on Alkylsilane
920 Self-Assembled Monolayers. *ACS Appl. Mater. Interfaces* **2017**, *9*, 11993–12002.
- 921 (60) Fernandez-Martinez, A.; Tao, J.; Wallace, A. F.; Bourg, I. C.; Johnson, M. R.; De Yoreo, J. J.;
922 Sposito, G.; Cuello, G. J.; Charlet, L. Curvature-Induced Hydrophobicity at Imogolite-Water
923 Interfaces. *Environ. Sci. Nano* **2020**, *7*, 2759–2772.
- 924 (61) Skelton, A. A.; Fenter, P.; Kubicki, J. D.; Wesolowski, D. J.; Cummings, P. T. Simulations of the
925 Quartz(1011)/Water Interface: A Comparison of Classical Force Fields, Ab Initio Molecular
926 Dynamics, and X-Ray Reflectivity Experiments. *J. Phys. Chem. C* **2011**, *115*, 2076–2088.
- 927 (62) Ferrage, E.; Sakharov, B. A.; Michot, L. J.; Delville, A.; Bauer, A.; Lanson, B.; Grangeon, S.;
928 Frappet, G.; Jiménez-Ruiz, M.; Cuello, G. J. Hydration Properties and Interlayer
929 Organization of Water and Ions in Synthetic Na-Smectite with Tetrahedral Layer Charge.
930 Part 2. Toward a Precise Coupling between Molecular Simulations and Diffraction Data. *J.*
931 *Phys. Chem. C* **2011**, *115*, 1867–1881.
- 932 (63) Wander, M. C. F.; Clark, A. E. Structural and Dielectric Properties of Quartz - Water
933 Interfaces. *J. Phys. Chem. C* **2008**, *112*, 19986–19994.
- 934 (64) Underwood, T. R.; Bourg, I. C. Large-Scale Molecular Dynamics Simulation of the
935 Dehydration of a Suspension of Smectite Clay Nanoparticles. *J. Phys. Chem. C* **2020**, *124*,
936 3702–3714.
- 937 (65) Etzold, M. A.; McDonald, P. J.; Routh, A. F. Growth of Sheets in 3D Confinements — a Model
938 for the C-S-H Meso Structure. *Cem. Concr. Res.* **2014**, *63*, 137–142.
939 <https://doi.org/https://doi.org/10.1016/j.cemconres.2014.05.001>.
- 940 (66) Jennings, H. M. Refinements to Colloid Model of C-S-H in Cement : CM-II. **2008**, *38*, 275–
941 289. <https://doi.org/10.1016/j.cemconres.2007.10.006>.
- 942 (67) Goret, G.; Aoun, B.; Pellegrini, E. MDANSE: An Interactive Analysis Environment for
943 Molecular Dynamics Simulations. *J. Chem. Inf. Model.* **2017**, *57* (1), 1–5.
944 <https://doi.org/10.1021/acs.jcim.6b00571>.
- 945 (68) Lothenbach, B.; Nonat, A. Calcium Silicate Hydrates: Solid and Liquid Phase Composition.
946 *Cem. Concr. Res.* **2015**, *78*, 57–70.
- 947 (69) L'Hôpital, E.; Lothenbach, B.; Le Saout, G.; Kulik, D.; Scrivener, K. Incorporation of

- Aluminium in Calcium-Silicate-Hydrates. *Cem. Concr. Res.* **2015**, 75, 91–103.
- (70) Richardson, I. G. The Calcium Silicate Hydrates. *Cem. Concr. Res.* **2008**, 38, 137–158.
- (71) L'Hôpital, E.; Lothenbach, B.; Kulik, D. A.; Scrivener, K. Influence of Calcium to Silica Ratio on Aluminium Uptake in Calcium Silicate Hydrate. *Cem. Concr. Res.* **2016**, 85, 111–121.
- (72) Allen, A. J.; Thomas, J. J.; Jennings, H. M. Composition and Density of Nanoscale Calcium-Silicate-Hydrate in Cement. *Nat. Mater.* **2007**, 6, 311–316.
- (73) Gregg, S. J.; Sing, K. S. W.; Salzberg, H. W. Adsorption Surface Area and Porosity. *J. Electrochem. Soc.* **1967**, 114 (11), 279C. <https://doi.org/10.1149/1.2426447>.
- (74) Thomas, J.; Jennings, H.; Allen, A. The Surface Area of Hardened Cement Paste as Measured by Various Techniques. *Concr. Sci. Eng.* **1999**, 1.
- (75) Mikhail, R. S.; Kamel, A. M.; Abo-El-Enein, S. A. Surface Properties of Cement Hydration Products. I. Pore Structure of Calcium Silicate Hydrates Prepared in a Suspension Form. *J. Appl. Chem.* **1969**, 19 (11), 324–328. <https://doi.org/10.1002/jctb.5010191105>.
- (76) Badmann, R.; Stockhausen, N.; Setzer, M. J. The Statistical Thickness and the Chemical Potential of Adsorbed Water Films. *J. Colloid Interface Sci.* **1981**, 82 (2), 534–542. [https://doi.org/10.1016/0021-9797\(81\)90395-7](https://doi.org/10.1016/0021-9797(81)90395-7).
- (77) Levchenko, A. A.; Kolesnikov, A. I.; Ross, N. L.; Boerio-Goates, J.; Woodfield, B. F.; Li, G.; Navrotsky, A. Dynamics of Water Confined on a TiO₂ (Anatase) Surface. *J. Phys. Chem. A* **2007**, 111 (49), 12584–12588. <https://doi.org/10.1021/jp076033j>.
- (78) Mitchell, P. C. H.; Parker, S. F.; Ramirez-Cuesta, A. J.; Tomkinson, J. *Vibrational Spectroscopy with Neutrons*; WORLD SCIENTIFIC, 2005; Vol. Volume 3. <https://doi.org/doi:10.1142/5628>.
- (79) Russo, D.; Teixeira, J.; Kneller, L.; Copley, J. R. D.; Ollivier, J.; Perticaroli, S.; Pellegrini, E.; Gonzalez, M. A. Vibrational Density of States of Hydration Water at Biomolecular Sites: Hydrophobicity Promotes Low Density Amorphous Ice Behavior. *J. Am. Chem. Soc.* **2011**, 133 (13), 4882–4888. <https://doi.org/10.1021/ja109610f>.
- (80) Monet, G.; Paineau, E.; Chai, Z.; Amara, M. S.; Orecchini, A.; Jimenez-Ruiz, M.; Ruiz-Caridad, A.; Fine, L.; Rouzière, S.; Liu, L. M.; Teobaldi, G.; Rols, S.; Launois, P. Solid Wetting-Layers in Inorganic Nano-Reactors: The Water in Imogolite Nanotube Case. *Nanoscale Adv.* **2020**, 2 (5), 1869–1877. <https://doi.org/10.1039/d0na00128g>.
- (81) Sheka, E. F.; Hołderna-Natkaniec, K.; Natkaniec, I.; Krawczyk, J. X.; Golubev, Y. A.; Rozhkova,

- 979 N. N.; Kim, V. V.; Popova, N. A.; Popova, V. A. Computationally Supported Neutron Scattering
980 Study of Natural and Synthetic Amorphous Carbons. *J. Phys. Chem. C* **2019**, *123* (25),
981 15841–15850. <https://doi.org/10.1021/acs.jpcc.9b03675>.
- 982 (82) Larsen, S. R.; Michels, L.; dos Santos, É. C.; Berg, M. C.; Gates, W. P.; Aldridge, L. P.; Seydel,
983 T.; Ollivier, J.; Telling, M. T. F.; Fossum, J. O.; Bordallo, H. N. Physicochemical
984 Characterisation of Fluorohectorite: Water Dynamics and Nanocarrier Properties.
985 *Microporous Mesoporous Mater.* **2020**, *306* (June), 110512.
986 <https://doi.org/10.1016/j.micromeso.2020.110512>.
- 987 (83) Chen, S. H.; Liao, C.; Sciortino, F.; Gallo, P.; Tartaglia, P. Model for Single-Particle Dynamics
988 in Supercooled Water. *Phys. Rev. E* **1999**, *59* (6), 6708–6714.
989 <https://doi.org/10.1103/PhysRevE.59.6708>.
- 990 (84) Cygan, R. T.; Daemen, L. L.; Ilgen, A. G.; Krumhansl, J. L.; Nenoff, T. M. Inelastic Neutron
991 Scattering and Molecular Simulation of the Dynamics of Interlayer Water in Smectite Clay
992 Minerals. *J. Phys. Chem. C* **2015**, *119* (50), 28005–28019.
993 <https://doi.org/10.1021/acs.jpcc.5b08838>.
- 994 (85) Elton, D. C.; Fernández-Serra, M. The Hydrogen-Bond Network of Water Supports
995 Propagating Optical Phonon-like Modes. *Nat. Commun.* **2016**, *7* (1), 10193.
996 <https://doi.org/10.1038/ncomms10193>.
- 997 (86) Zhou, T.; Ioannidou, K.; Ulm, F.-J.; Bazant, M. Z.; Pellenq, R. J. M. Multiscale Poromechanics
998 of Wet Cement Paste. *Proc. Natl. Acad. Sci.* **2019**, *116*, 10652–10657.
- 999 (87) Bonnaud, P. A.; Coasne, B.; Pellenq, R. J. M. Solvated Calcium Ions in Charged Silica
1000 Nanopores. *J. Chem. Phys.* **2012**, *137*.
- 1001 (88) Odler, I. The BET-Specific Surface Area of Hydrated Portland Cement and Related
1002 Materials. **2003**, *33*, 2049–2056.
- 1003 (89) Beaudoin, J.; Odler, I. *Hydration, Setting and Hardening of Portland Cement*, 5th ed.; Hewlett,
1004 P., Liska, M., Eds.; Elsevier Ltd.: Oxford, U.K., 2019.
- 1005 (90) Grangeon, S.; Claret, F.; Lerouge, C.; Warmont, F.; Sato, T.; Anraku, S.; Numako, C.; Linard,
1006 Y.; Lanson, B. On the Nature of Structural Disorder in Calcium Silicate Hydrates with a
1007 Calcium/Silicon Ratio Similar to Tobermorite. *Cem. Concr. Res.* **2013**, *52*, 31–37.
1008 <https://doi.org/https://doi.org/10.1016/j.cemconres.2013.05.007>.
- 1009 (91) Li, B.; Li, N.; Brouwers, H. J. H.; Yu, Q.; Chen, W. Understanding Hydrogen Bonding in
1010 Calcium Silicate Hydrate Combining Solid-State NMR and First Principle Calculations.

1011 *Constr. Build. Mater.* **2020**, 233, 117347.
 1012 <https://doi.org/https://doi.org/10.1016/j.conbuildmat.2019.117347>.

1013 (92) Grangeon, S.; Claret, F.; Roosz, C.; Sato, T.; Gaboreau, S.; Linard, Y. Structure of
 1014 Nanocrystalline Calcium Silicate Hydrates: Insights from X-Ray Diffraction, Synchrotron X-
 1015 Ray Absorption and Nuclear Magnetic Resonance. *J. Appl. Crystallogr.* **2016**, 49, 771–783.
 1016 <https://doi.org/10.1107/S1600576716003885>.

1017 (93) Cong, X.; Kirkpatrick, R. J. ^1H — ^{29}Si CP/MAS NMR Study of the Structure of Calcium Silicate
 1018 Hydrate. *Adv. Cem. Based Mater.* **1996**, 3, 144–156.

1019 (94) Asta, M. P.; Fernandez-Martinez, A.; Alonso, J.; Charlet, L.; Findling, N.; Magnin, V.; Ruta, B.;
 1020 Sprung, M.; Westermeier, F. Nanoscale Ion Dynamics Control on Amorphous Calcium
 1021 Carbonate Crystallization: Precise Control of Calcite Crystal Sizes. *J. Phys. Chem. C* **2020**,
 1022 124 (46), 25645–25656. <https://doi.org/10.1021/acs.jpcc.0c08670>.

1023 (95) Pachon-Rodriguez, E. A.; Guillon, E.; Houvenaghel, G.; Colombani, J. Wet Creep of Hardened
 1024 Hydraulic Cements — Example of Gypsum Plaster and Implication for Hydrated Portland
 1025 Cement. *Cem. Concr. Res.* **2014**, 63, 67–74.
 1026 <https://doi.org/https://doi.org/10.1016/j.cemconres.2014.05.004>.

1027

1028